

Chapter 13

Wireless Intraocular Microrobots: Opportunities and Challenges

Olgaç Ergeneman, Christos Bergeles, Michael P. Kummer,
Jake J. Abbott, and Bradley J. Nelson

Abstract Many current and proposed retinal procedures are at the limits of human performance and perception. Microrobots that can navigate the fluid in the interior of the eye have the potential to revolutionize the way the most difficult retinal procedures are conducted. Microrobots are typically envisioned as miniature mechatronic systems that utilize MEMS technology to incorporate sensing and actuation onboard. This chapter presents a simpler alternative approach for the development of intraocular microrobots consisting of magnetic platforms and functional coatings. Luminescence dyes immobilized in coatings can be excited and read wirelessly to detect analytes or physical properties. Drug coatings can be used for diffusion-based delivery, and may provide more efficient therapy than microsystems containing pumps, as diffusion dominates over advection at the microscale. Oxygen sensing for diagnosis and drug therapy for retinal vein occlusions are presented as example applications. Accurate sensing and therapy requires precise control to guide the microrobot in the interior of the human eye. We require an understanding of the possibilities and limitations in wireless magnetic control. We also require the ability to visually track and localize the microrobot inside the eye, while obtaining clinically useful retinal images. Each of these topics is discussed.

Keywords Eye · Microrobot · Minimally invasive surgery · Magnetic control · Wireless · Tracking · Localizing · Ophthalmoscopy · Intraocular · Luminescence · Coatings · Drug delivery · Drug release · Sensing

O. Ergeneman (✉)

Institute of Robotics and Intelligent Systems, ETH Zurich, Tannenstr. 3, CLA H 17.1,
8092 Zurich, Switzerland
e-mail: oergeneman@ethz.ch

13.1 Introduction

During the past decade, the popularity of minimally invasive medical diagnosis and treatment has risen remarkably. Further advances in biomicrobotics will enable the development of new diagnostic and therapeutic systems that provide major advantages over existing methods. Microrobots that can navigate bodily fluids will enable localized sensing and targeted drug delivery in parts of the body that are currently inaccessible or too invasive to access.

Microelectromechanical systems (MEMS) technology has enabled the integration of sensors, actuators, and electronics at microscales. In recent years, a great deal of progress has been made in the development of microdevices, and many devices have been proposed for different applications. However, placing these systems in a living body is limited by factors like biocompatibility, fouling, electric hazard, energy supply, and heat dissipation. In addition, the development of functional MEMS devices remains a time-consuming and costly process. Moving micro-sized objects in a fluid environment is also challenging, and a great deal of research has considered the development of microactuators for the locomotion of microrobots. However, to date the most promising methods for microrobot locomotion have utilized magnetic fields for wireless power and control, and this topic is now well understood [2, 28, 32, 49, 66]. A large number of micropumps have been developed for drug delivery, but as size is reduced diffusion begins to dominate over advection, making transport mechanisms behave differently at small scales. Consequently, future biomedical microrobots may differ from what is typically envisioned.

In this chapter we focus on intraocular microrobots. Many current and proposed retinal procedures are at limits of human performance and perception. Microrobots that can navigate the fluid in the interior of the eye have the potential to revolutionize the way the most difficult retinal procedures are conducted. The proposed devices can be inserted in the eye through a small incision in the sclera, and control within the eye can be accomplished via applied magnetic fields. In this chapter we consider three topics in the design and control of intraocular microrobots: First, we discuss functional coatings – both for remote sensing and targeted drug delivery. Next, we discuss magnetic control, and the ability to generate sufficient forces to puncture retinal veins. Finally, we discuss visually tracking and localizing intraocular microrobots. The eye is unique in that it is possible to observe the vasculature and visually track the microrobot through the pupil.

Throughout this chapter, we consider the assembled-MEMS microrobots as shown in Fig. 13.1, but the conclusions extend to other microrobot designs. Fabricating truly 3-D mechanical structures at the microscale is challenging. With current MEMS fabrication methods, mechanical parts are built using 2-D (planar) geometries with desired thickness. Three-dimensional structures can be obtained by bending or assembling these planar parts, and it has been demonstrated that very complex structures can be built with such methods [33, 59, 65, 66]. The philosophy of designing simple structures with no actuation or intelligence onboard begs the

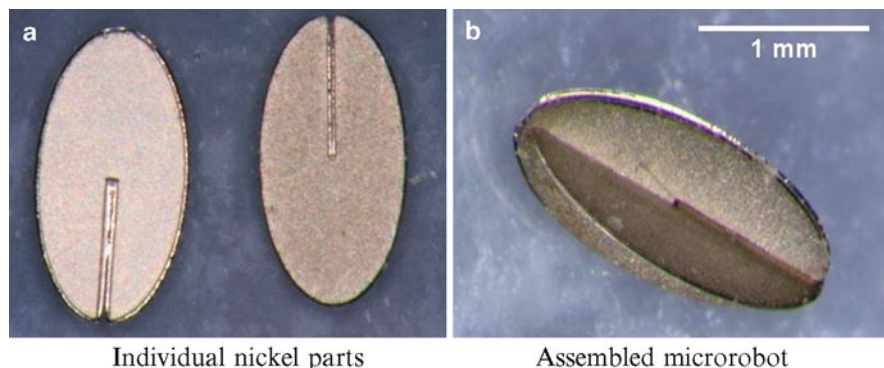


Fig. 13.1 Relatively simple 2-D parts can be assembled into complex 3-D structures (©IEEE 2008), reprinted with permission. The parts shown have dimensions $2.0\text{ mm} \times 1.0\text{ mm} \times 42\text{ }\mu\text{m}$ and can be further miniaturized

question: Are these devices microrobots? It may be more accurate to think of these devices as end-effectors of novel manipulators where magnetic fields replace mechanical links, sensing is performed wirelessly, and system intelligence is located outside of the patient. However, this matter of semantics is inconsequential if the goal is to develop functional biomedical microdevices.

13.2 Functionalizing Microrobots with Surface Coatings

We present an alternative approach for the development of biomicrobots utilizing a magnetic platform and functional coatings for remote sensing and targeted drug delivery (Fig. 13.2). Coatings possessing sensor properties or carrying drugs may be superior to more complicated electromechanical systems. Luminescence dyes immobilized in coatings can be excited and read out wirelessly for detecting analytes or physical properties. Drugs coated on a carrier can be used for diffusion-based delivery and may provide more efficient therapy than microsystems containing pumps. Because of the discrepancy in scaling of volume and surface area, reservoirs built inside microfabricated devices may be insufficient, whereas surface coatings alone may provide sufficient volume. Fabrication of devices utilizing coatings will also be simple compared to systems with many electrical or mechanical components. All of these properties make wireless microrobots consisting of magnetic bodies and functional coatings feasible in the near term.

13.2.1 Biocompatibility Coatings

Magnetic microrobots contain nickel, cobalt, iron, or their alloys. These elements and their alloys are declared to be non-biocompatible. Hence, they are not used in

Fig. 13.2 Microrobot utilizing a functional coating (©IEEE 2008), reprinted with permission. *Right:* A bare magnetic microrobot made of thin assembled nickel pieces, based on [66]. *Left:* A microrobot coated with an oxygen-sensitive film



medical devices. Ti and Ti-alloys are used extensively in biomedical applications because of their excellent combination of biocompatibility, corrosion resistance, and structural properties [51]. In order to achieve biocompatibility without sacrificing the magnetic properties, microrobot pieces can be coated with a thin layer of Ti, forming a titanium dioxide layer once exposed to air.

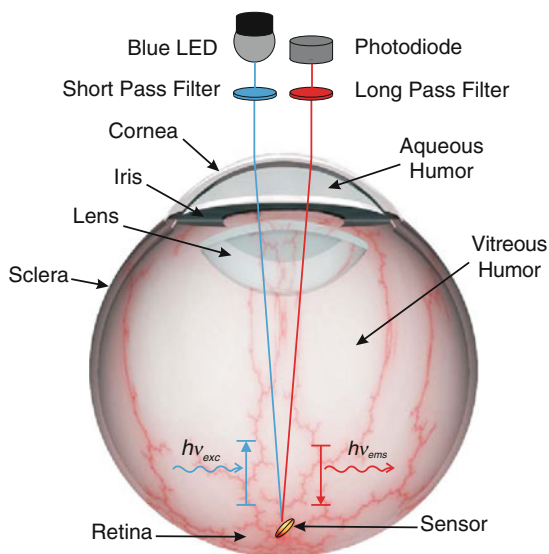
In [17] microrobot pieces made of Ni are coated by Ti with thicknesses of 100 nm, 200 nm, 300 nm, and 500 nm using a DC sputterer. Biocompatibility covers a broad spectrum of non-toxic and non-allergic properties, with various levels of biocompatibility associated with the purpose of a medical device. Biocompatibility tests involve toxicity tests, corrosion tests, and allergy tests. To validate the quality of coatings, against possible faults and crack formations, in vitro direct-contact cell-toxicity tests, in line with ISO 10993-5 8.3 standard, were performed on coated and uncoated microrobots using NIH 3T3 fibroblast cells. Results show that as thin as a 100-nm-thick Ti coating is sufficient to obtain biocompatibility.

13.2.2 Coatings for Remote Sensing

Surface coatings can be used to fabricate minimally invasive wireless sensor devices, such as the intraocular sensor depicted in Fig. 13.3. The proposed device consists of a luminescence sensor film that is integrated with a magnetically controlled platform. This system can be used to obtain concentration maps of clinically relevant species (e.g., oxygen, glucose, urea, drugs) or physiological parameters (e.g., pressure, pH, temperature) inside the eye, specifically in the preretinal area. Effects of specific physiological conditions on ophthalmic disorders can be conveyed.

These devices can also be used in the study of pharmacokinetics as well as in the development of new drug delivery mechanisms, as summarized below [48].

Fig. 13.3 Artist's conception of the magnetically controlled wireless sensor in the eye (©IEEE 2008), reprinted with permission [21]



The study of pharmacokinetics of drugs that diffuse into the eye following intraocular drug injection requires analysis of ocular specimens as they change in time. The risk of iatrogenic complications when penetrating into the ocular cavity with a needle has restricted ocular pharmacokinetic studies on animals and humans. Microdialysis has become an important method for obtaining intraocular pharmacokinetic data and it has reduced the number of animals needed to estimate ocular pharmacokinetic parameter values. However, the insertion of the probe and anesthesia have been shown to alter the pharmacokinetics of drugs. The microrobotic system presented here can replace microdialysis probes for obtaining intraocular pharmacokinetic data as it provides a minimally invasive alternative for in vivo measurements of certain analytes. Concentration as a function of time and position can be obtained by steering the magnetic sensor inside the vitreous cavity. Knowledge of concentration variations within the vitreous will expedite the optimization of drug administration techniques for posterior segment diseases.

13.2.2.1 Luminescence Sensing

Photoluminescence is the emission of electromagnetic radiation (i.e. photons) from a material in response to absorption of photons. The intensity and the lifetime of emission can be decreased by a variety of processes referred to as luminescence quenching.

Optical luminescence sensors work based on quenching of luminescence in the presence of a quencher (i.e., analyte of interest); the decrease in luminescence is related to the quantity of the quencher. A number of devices using this principle have been demonstrated and the basic principles of different methods can be found in [40]. The quenching of luminescence is described by Stern-Volmer equations:

$$\frac{I_0}{I} = 1 + K[Q] \quad (13.1)$$

$$\frac{\tau_0}{\tau} = 1 + K[Q] \quad (13.2)$$

where I_0 and I are the luminescence intensities in the absence and in the presence of quencher, respectively, τ_0 and τ are the luminescence lifetimes in the absence and presence of quencher, respectively, $[Q]$ is the quencher concentration, and K is the Stern-Volmer quenching constant whose units are the reciprocal of the units of $[Q]$. Luminescence dyes with high quantum yield, large dynamic range, and large Stokes shift are preferred for luminescence sensors. To be used as a sensor, these dyes need to be immobilized. They are usually bound to transparent and quencher-permeable supporting matrices such as polymers, silica gels, or sol-gels. Quencher permeability, selectivity, and the luminophore solubility are the important factors for choosing appropriate supporting matrices.

Luminescence sensing can be done either based on luminescence intensity or luminescence lifetime. The main difference between the two methods is that intensity is an extrinsic property whereas lifetime is an intrinsic property. Extrinsic techniques depend on parameters such as the dye concentration, optical surface quality, photo-bleaching, and incidence angle, which change from sample to sample. When the sensor's position changes, the optical path distance (OPD) from the light source to the sensor and back to the photo detector changes. The total amount of light collected by the sensor changes depending on the OPD and orientation. These quantities are hard to control in such a wireless sensor application, limiting the accuracy of this technique. Intrinsic properties do not depend on the parameters described above, making lifetime measurements more promising for wireless microrobotic applications.

There are two methods that are used for measuring luminescence lifetimes: time-domain measurements and frequency-domain measurements. In time-domain measurements the sample is excited with light pulses, and the intensity signal that changes as a function of time is measured and analyzed. In frequency-domain measurements the sample is excited with a periodic signal that consequently causes a modulated luminescence emission at the identical frequency. Because of the lifetime of emission, the emission signal has a phase shift with respect to the excitation signal. The input excitation signal is used as a reference to establish a zero-phase position and the lifetime is obtained by measuring the phase shift between the excitation and emission signals.

13.2.2.2 An Intraocular Oxygen Sensor

The retina needs sufficient supply of oxygen and other nutrients to perform its primary visual function. Inadequate oxygen supply (i.e. retinal hypoxia) is correlated with major eye diseases including diabetic retinopathy, glaucoma, retinopathy of prematurity, age-related macular degeneration, and retinal vein occlusions [25]. Retinal hypoxia is presumed to initiate angiogenesis, which is a major cause of blindness in developed countries [14]. Attempts to test this hypothesis suffer from the current methods of highly invasive oxygen electrodes. Hypoxia is typically present at the end stages of retinal diseases. However, during the early stages, the relation between blood flow sufficiency, vessel patency, and tissue hypoxia are still unknown [55]. The influence of oxygen on these diseases is not well understood and the ability to make long-term, non-invasive, in vivo oxygen measurements in the human eye is essential for better diagnosis and treatment. Measuring the oxygen tensions both in aqueous humor and vitreous humor, and particularly in the pre-retinal area, is of great interest in ophthalmic research.

To address these issues, an intraocular optical oxygen sensor utilizing a luminescence coating has been developed [21]. The sensor works based on quenching of luminescence in the presence of oxygen. A novel iridium phosphorescent complex is designed and synthesized to be used as the oxygen probe. The main advantages of this iridium complex, when compared to other metal complexes, are its higher luminescence quantum yield, higher photo-stability, longer lifetime, stronger absorption band in the visible region, and larger Stokes shift. Polystyrene is chosen as the supporting matrix because of its high oxygen permeability and biocompatible nature. The microrobots are dip-coated with polystyrene film containing luminescence dye, and good uniformity is achieved across the magnetic body. Biocompatibility tests must still be performed on the polystyrene film with embedded dye. If needed, an additional layer of pure polystyrene could be added to isolate the sensing layer.

An experimental setup has been built to characterize the oxygen sensitivity of the sensor. The details of the sensor and characterization setup can be found in [21]. A blue LED is used as the excitation source for the oxygen sensor system and a photodiode is used to detect the luminescence. Optical filters are used to separate the emission signal from the excitation signal. The frequency-domain lifetime measurement approach is used in this work. De-ionized water is used for the dissolved oxygen measurements. The sensor's location in the setup is maintained with a magnet. The distances between the components and the sensor are chosen considering the geometry of the eye. A range of oxygen concentrations is achieved by bubbling air or nitrogen gas. Nitrogen replaces oxygen molecules in the solution, and air provides oxygen. Figure 13.4 shows the Stern-Volmer plot as a function of oxygen concentration. As seen in this figure, a linear model proved to be an excellent predictor ($R^2 = 0.989$) for oxygen concentrations compared to a commercial sensor.

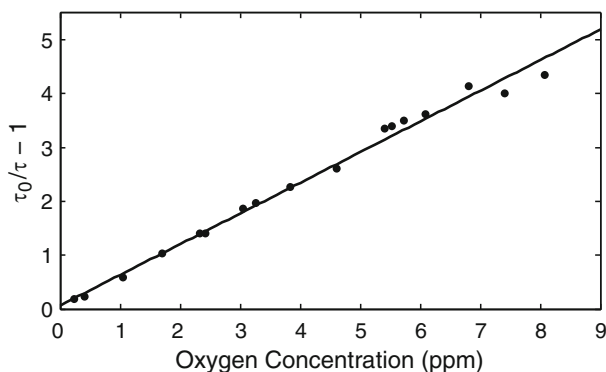
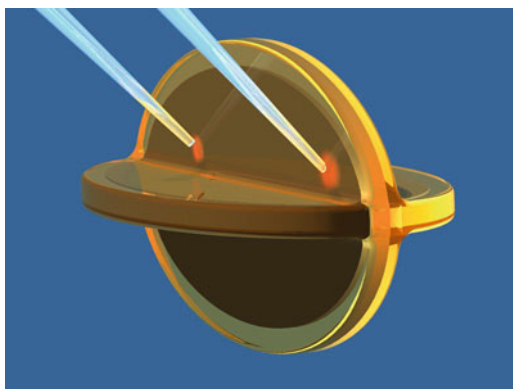


Fig. 13.4 Stern-Volmer plot of the luminescence dyes immobilized in polystyrene film under various oxygen concentrations (©IEEE 2008), reprinted with permission [21]

Fig. 13.5 Measurement of local gradients is possible exciting and reading out from different parts of the microrobot (©IEEE 2008), reprinted with permission



13.2.2.3 Measuring Gradients

It may be desirable to measure spatial gradients in a quantity. This can be accomplished by taking measurements while moving the microrobot. However, these measurements will be separated in time, and the movement of the microrobot could potentially affect the environment, particularly in a low-Reynolds-number regime. It is possible to measure gradients directly with a stationary microrobot. Specific locations on the microrobot can be excited and sensed simultaneously, as depicted in Fig. 13.5. This requires the ability to focus the excitation signal on a specific region of the microrobot. Clearly, this necessitates a greater level of sensing spatial resolution. Alternatively, multiple dyes with different emission spectra can be excited simultaneously, and the emitted signals can be band-pass filtered.

13.2.3 Coatings for Targeted Drug Delivery

The main challenge of ophthalmic drug delivery is to keep desired drug concentrations in the target area for the desired duration, while minimizing the drug levels in the remainder of the body. To date, a variety of drug delivery approaches have been shown to be effective therapeutically. Some salient findings from [48] are summarized below. Ocular delivery can be achieved by topical administration, systemic administration, periocular injections, and intraocular injections. Depending on the target area, drug delivery can be achieved by penetrating through the cornea, conjunctiva, or sclera following topical administration (i.e. eye drops), or across blood-aqueous barrier along with blood-retinal barrier following systemic administration. Only a minute fraction of applied dose reaches the intraocular target area after topical and systemic administration. Drug delivery using gelatin wafers, collagen shields, and soft contact lenses placed on the cornea or in the cul-de-sac have been tested, as well as methods like iontophoresis. Drug delivery for posterior-segment disorders (e.g. diabetic retinopathy, macular degeneration, retinal edema, retinal vein occlusions) has always been a challenge as it requires access to the retina and the choroid. Periocular injections and intraocular injections place the drug closer to the target tissue, overcoming some of the ocular barriers. Many of the drugs used to treat vitreous and retinal disorders have a narrow concentration range in which they are effective, and they may be toxic at higher concentrations. Slight changes in injection conditions (e.g. position, shape) will produce different drug concentrations within the vitreous, and therefore the efficacy of the treatment produced by the drug can be sensitive to injection conditions. Intraocular injections have also been associated with serious side effects, such as endophthalmitis, cataract, hemorrhage, and retinal detachment [26], and long-duration drug delivery is not possible with these methods.

New drug-delivery methods provide many advantages compared to the traditional methods. However, it is not always possible to deliver drugs to the target tissue with existing methods. Superior methods for targeted drug delivery are needed, and robotic assistance in drug delivery will have major benefits. Devices inserted into the aqueous or vitreous cavity bear great potential for drug delivery. Recently, methods to deliver drugs using carriers such as liposomes, gels, and nanoparticles have been evaluated. Methods to achieve desired concentrations over long periods of time using drugs that become active inside the eye (prodrugs) are also being investigated. Controlled-release devices and biodegradable implants can increase the effectiveness of these devices.

At the microscale, diffusion becomes the dominant mechanism for mass transport. Low-Reynolds-number flow is laminar, and the lack of turbulent mixing puts a diffusion limit on drug delivery using micropumps. In [17] an alternative approach to targeted drug delivery is proposed: wireless magnetic microrobots surface coated with drug. The microrobot will be steered to the site of action and it will be kept at this position as the drug is released from the microrobot by diffusion.

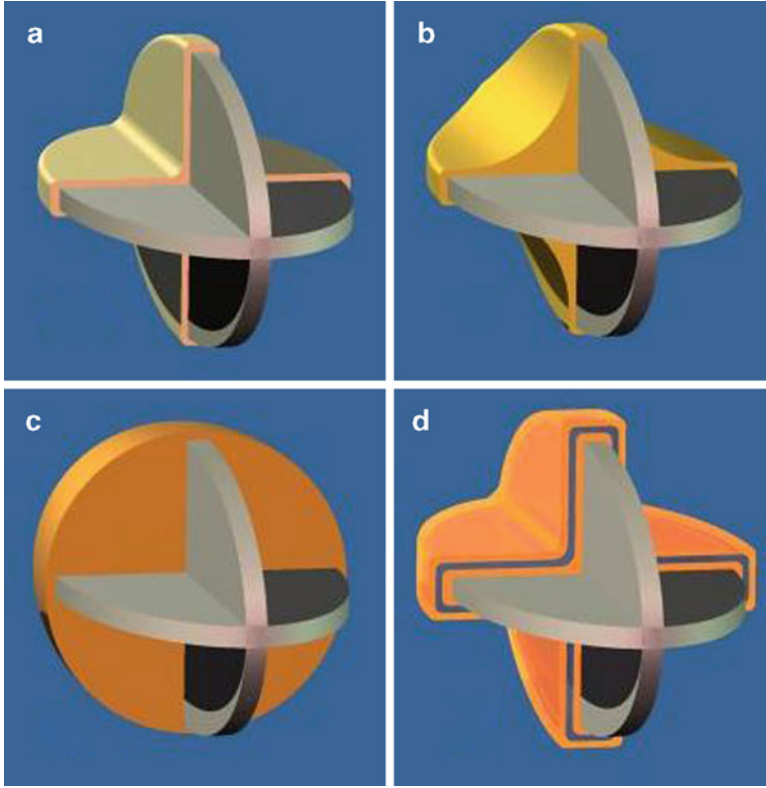


Fig. 13.6 Drug coatings can range from thin surface coatings to coatings that take advantage of the total available volume created by the microrobot structure. Coatings are shown only at the back part of the microrobot (©IEEE 2008), reprinted with permission

13.2.3.1 Quantity of Coated Drug

Carrying drug by surface coating becomes more desirable as size is reduced (Fig. 13.6). Consider an assembled microrobot like those shown in Fig. 13.2. The microrobot can be modeled by two elliptical pieces of magnetic material of length $2a$, width $2b$, and thickness c , and by a circular piece of diameter $2b$ and thickness c . The volume of the magnetic structure is calculated as

$$v_s = (2\pi ab + \pi b^2)c - (2a + 4b)c^2 + c^3 \quad (13.3)$$

The microrobot has a volumetric footprint of an ellipsoid of volume

$$v_e = \frac{4}{3}\pi ab^2 \quad (13.4)$$

If we consider a coating of drug that fills in the entire ellipsoidal volumetric footprint of the microrobot (similar to Fig. 13.6c), the volume of drug carried is simply the volume of the ellipsoid minus the volume of the magnetic structure

$$v_f = v_e - v_m \quad (13.5)$$

If we consider a single thin surface coating of thickness t , (similar to Fig. 13.6a), the volume of drug carried is given by

$$v_t = (4\pi ab + 2\pi b^2)t - (8a + 16b - 12c)t^2 + 8t^3 \quad (13.6)$$

Figure 13.7 shows the effect of scaling on the ability to carry drug by surface coating. For even relatively large microrobots, the amount of drug carried on the surface with a single thin coating is comparable to the total volume of the magnetic structure. As the size of the microrobot is reduced, the volume of drug in a single thin coating becomes comparable to the total ellipsoidal volume of the microrobot. In practice, any fabricated reservoir could only amount to a fraction of the total volume of the structure, and the drug would need to be in solution (that is, diluted) in order to be pumped. The ability to surface coat highly concentrated drug increases the benefits of surface coatings even beyond what is observed in Fig. 13.7.

In order to bind more proteins or drugs onto a microrobot of the same surface area, multilayer surface coatings or coatings embedded in different base matrices should be developed (Fig. 13.6d). Among others, hydrogels, agarose, starch microcapsulations, polymer matrices, liposomes, and biodegradable needles are widely used for making drug delivery matrices that can hold much more drug due to their material properties [15, 50]. These materials can be used to encapsulate drug

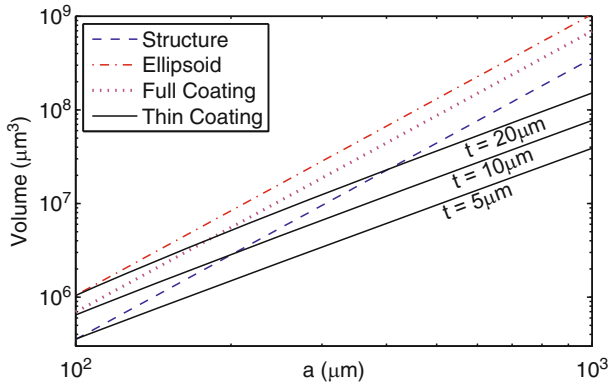


Fig. 13.7 Effect of scaling on volume with microrobots of the type shown in Fig. 13.2 (©IEEE 2008), reprinted with permission. Curves correspond to (3)–(6), respectively, with $b = a/2$ and $c = a/10$

molecules as an outer coating, enabling multilayer coatings. These multilayer coatings can be used to coat multiple drug types on one microrobot, or used to fine tune delivery times or dosage. Alternatively, embedding drug molecules in a porous matrix facilitates slower diffusion and more drug loading capacity. Controlled release of drugs has been demonstrated using intelligent polymers that respond to stimuli such magnetic fields, ultrasound, temperature, and pH. They enable fine tuning of diffusive drug release.

13.2.3.2 Drug Delivery for Retinal Vein Occlusions

Retinal vein occlusion (RVO) is a common retinovascular disease caused by obstruction of blood flow due to clot formation. RVO is among the most common causes of vision loss around the world, with one study reporting a prevalence of 1.6% in adults aged 49 years or older [60]. Various treatment methods for RVO have been proposed and attempted, however to date there is no effective clinical treatment for RVO. Among these methods, prolonged local intravenous thrombolysis (i.e., clot dissolution) with tissue plasminogen activator (t-PA) injection is the most promising treatment [53], based on excessive postoperative complications or inconclusive clinical trials of other methods.

Retinal drug delivery by injections requires precise manipulation that is constrained by the limits of human performance and perception [34]. Retinal veins are small delicate structures surrounded by fragile retinal tissue, and prolonged manual cannulation of retinal veins risks causing permanent damage to the retina. Robotic systems have been proposed to assist with retinal vein cannulation, utilizing robot-assisted surgical instruments that pass through a hole in the sclera as in conventional vitreoretinal surgery [47, 52].

In [17] an alternative approach to RVO treatment is proposed: a wireless magnetic microrobot coated with clot-dissolving t-PA. The microrobot will be steered to the thrombus site as it is tracked visually through the pupil, and will be immobilized in close proximity of the retinal veins. Immobilization can be achieved by puncturing and docking to a retinal vein. Diffusion of t-PA from the surface coating of the microrobot into the clotted region will start clot dissolution. There is strong evidence that t-PA in the preretinal area can diffuse into the retinal vasculature and break clots [27]. Since t-PA is an enzyme, and the clot dissolution reaction rate depends on enzyme reaction rate, long-term release of t-PA is thought to be more effective than bolus injections [43]. The proposed delivery mechanism provides drug release without the need for a micropump, and an efficient therapy using small amounts of t-PA over prolonged periods. Moreover, a microrobot is potentially less invasive than other methods, and has the potential to be left in the eye for extended periods of time, even in an outpatient scenario. However, it is not yet known what quantity of t-PA is required to effectively dissolve a clot using the proposed method.

13.2.3.3 Preliminary Drug Release Experiments

This section presents the results of preliminary drug release experiments using the untethered microrobot and discusses the feasibility of microrobotic drug delivery. A drug substitute is coated on microrobots in [17], the release kinetics is characterized, and the amount of drug that can be coated in a single layer on a microrobot is quantified.

In order to analyze the release kinetics of a diffusion-based drug delivery microrobot, in vitro experiments are conducted. As the drug molecule substitute, bovine serum albumin (BSA) was chosen. BSA is a plasma protein that can be used as a blocking agent or added to diluents in numerous biochemical applications. BSA is used because of its stability, its inert nature in many biochemical reactions, its representative molecular size, and its low cost.

Four elliptical microrobot pieces of length 900 μm , width 450 μm , and thickness 50 μm are used as the magnetic platform holding the coating. The pieces are made from electroplated nickel and then coated with titanium for biocompatibility. The pieces are first sterilized and then placed in different wells of a 96-well culture plate. A sterilized BSA-solution of 3 mg/mL is prepared and labeled with Alexa-Fluor-546 (Molecular Probes) fluorescent marker. This solution is then mixed with sterilized PBS in order to create solutions with different concentrations of labeled-BSA molecules. Three of the microrobot pieces are dipped in BSA concentrations of 3 mg/mL, 2 mg/mL, 1 mg/mL, respectively, and one is dipped into a pure PBS solution, which contained no BSA, as a control set. The pieces are left in the solutions to allow the BSA to bind to the microrobot. The surface-coating process is done for 12 h at room temperature in a humidity chamber.

Coated microrobot pieces are taken from coating wells and placed in new wells filled with 200 μL PBS each. Following that, the fluorescence intensity is measured in set time intervals for three days using an automated spectrum analyzer. In this way, the kinetics of diffusion-based drug delivery with surface-coated microrobots are obtained.

Figure 13.8 quantifies the amount of time required to release the drug through diffusion, and it also gives qualitative information about the kinetics of release. It is clear that the concentration of the coating solution does not affect the amount of drug bound to the surface. This provides strong evidence that the amount of drug will be limited by the surface area of the microrobot.

Next, the amount of BSA released from a single layer on a single piece is quantified. The release wells of the culture plates are analyzed in the multiwell plate reader for fluorescence and absorbance values. The BSA standard concentration curve is obtained by preparing a Bradford Assay with ten different known concentrations of BSA in 1:2 dilutions, and analyzing this assay for fluorescence and absorbance. The obtained standard curve is used to calibrate the multiwell plate reader. The fluorescence intensity in the release wells is measured and, using the calibration curve, the amount of BSA released is found to be $2.5 \pm 0.1 \mu\text{g}$.

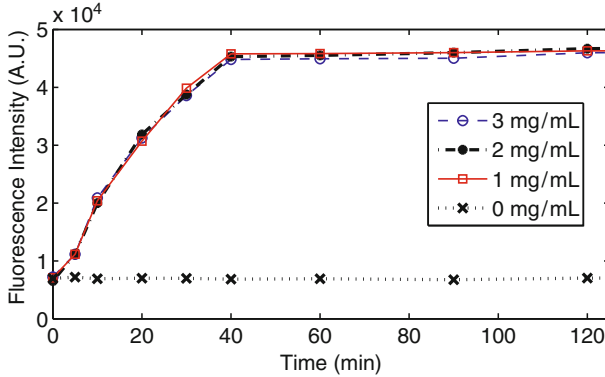


Fig. 13.8 Fluorescence intensity vs. time for the release experiment (©IEEE 2008), reprinted with permission [17]

13.3 Magnetic Control

One approach to the wireless control of microrobots is through externally applied magnetic fields [3]. There is a significant body of work dealing with non-contact magnetic manipulation [28]. Research has considered the 3-D positioning of permanent magnets [29, 36]. Magnetic fields have been used to orient small permanent magnets placed at the distal tips of catheters [1, 62]. Researchers have considered the position control of soft-magnetic beads as well, where a spherical shape simplifies the control problem [6]. The precision control of non-spherical soft-magnetic bodies has also been considered [2]. In addition to magnetic manipulation of simple objects (e.g., beads, cylinders), it is possible to manipulate more complicated shapes. In [66], a soft-magnetic assembled-MEMS microrobot is controlled by applying decoupled magnetic torque and force. Assembled-MEMS microrobots have the potential to provide increased functionality over simpler geometries. Controlled magnetic fields can be generated by stationary current-controlled electromagnets [45, 67], by electromagnets that are position and current controlled [29, 66s], or by position-controlled permanent magnets, such as with the Stereotaxis NIOBE Magnetic Navigation System, or even by a commercial MRI system [44]. In all cases, the rapid decay of magnetic field strength with distance from its source creates a major challenge for magnetic control.

Surgeons have been using magnets to remove metallic debris from eyes for over 100 years [9]. However, there has been no prior work of controlled magnetic manipulation of an object that has been intentionally inserted in the eye. Intraocular procedures are unique among *in vivo* procedures, as they provide a direct line of sight through the pupil for visual feedback, making closed-loop control possible.

If we want to apply controlled torques and forces to an object with magnetization \mathbf{M} (A/m) using a controlled magnetic field \mathbf{B} (T) the resulting equations for torque

and force are as follows [35]. The magnetic torque, which tends to align the magnetization of the object with the applied field:

$$\mathbf{T} = v\mathbf{M} \times \mathbf{B} \quad (13.7)$$

in units $\text{N} \cdot \text{m}$ where v is the volume of the body in m^3 . The force on the object is:

$$\mathbf{F} = v(\mathbf{M} \cdot \nabla)\mathbf{B} \quad (13.8)$$

in units N , where ∇ is the gradient operator:

$$\nabla = \left[\frac{\partial}{\partial x} \quad \frac{\partial}{\partial y} \quad \frac{\partial}{\partial z} \right]^T \quad (13.9)$$

Since there is no electric current flowing through the region occupied by the body, Maxwell's equations provide the constraint $\nabla \times \mathbf{B} = \mathbf{0}$. This allows us to express (8), after some manipulation, in a more intuitive and useful form:

$$\mathbf{F} = v \begin{bmatrix} \frac{\partial}{\partial x} \mathbf{B}^T \\ \frac{\partial}{\partial y} \mathbf{B}^T \\ \frac{\partial}{\partial z} \mathbf{B}^T \end{bmatrix} \mathbf{M} \quad (13.10)$$

The magnetic force in any given direction is the dot product of 1) the derivative of the field in that direction and 2) the magnetization.

We can also express the applied magnetic field's flux density as an applied magnetic field \mathbf{H} with units A/m . \mathbf{B} is related to \mathbf{H} simply as $\mathbf{B} = \mu_0 \mathbf{H}$ with $\mu_0 = 4\pi \times 10^{-7} \text{ T} \cdot \text{m/A}$, since air and biological materials are effectively nonmagnetic. Both (7) and (8) are based on the assumption that the magnetic body is small compared to spatial changes in the applied magnetic field's flux density, such that the applied flux density is fairly uniform across the body, and \mathbf{B} is the value at the center of mass of the body. It has been verified experimentally that this assumption gives an accurate prediction of magnetic force and torque [2, 49].

If the body of interest is a permanent magnet, the average magnetization \mathbf{M} is effectively independent of the applied magnetic field. The magnetization of a permanent magnet is governed by the remanent magnetization of the material and geometry of the body. This makes the calculation of torque and force acting on a permanent magnetic body straightforward as long as the magnetization and orientation of the body is known. The torque can be increased by increasing the angle between \mathbf{B} and \mathbf{M} , up to 90° , or by increasing the strength of \mathbf{B} . The force can be increased by increasing the gradients in the applied magnetic field.

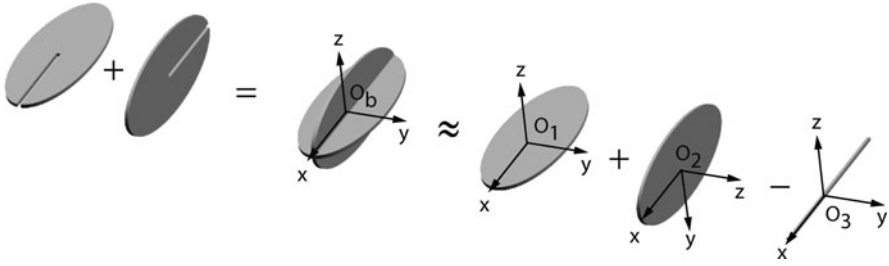


Fig. 13.9 Microfabricated nickel parts (*left*) are assembled to form a microrobot (*middle*). The body frame is assigned to the microrobot arbitrarily. For the computation, rather than using the actual complex shapes of the parts, we consider the microrobot as a superposition of simpler geometries (*right*). The frames of the individual parts are assigned with the x -axis along the longest dimension of the body and with the z -axis along the shortest dimension (©IEEE 2008), reprinted with permission [49]

If the body of interest is made of a soft-magnetic material, the magnetization is a nonlinear function of the applied field, with a magnitude limited by the saturation magnetization for the magnetic material, and can rotate with respect to the body. The governing equations for control are significantly more complex [2]. We sometimes refer to the magnetic moment or magnetic dipole moment, which represent the total strength of a magnet (hard or soft). The magnetic moment is simply the product of the volume v and the average magnetization \mathbf{M} .

The magnetization of a body depends on its shape, so bodies made of the same material but having different shapes will have different magnetization characteristics. The magnetization characteristics also differ along different directions within the body. This is known as shape anisotropy. Demagnetizing fields that tend to weaken magnetization create the shape anisotropy. Demagnetizing fields are largest along short directions of the body. A long direction in a body is referred to as an easy axis, since it is a relatively easy direction to magnetize the body. In general, the longest dimension of a soft-magnetic body will tend to align with the direction of the applied field. Other types of anisotropy exist, such as crystalline anisotropy, but these are typically negligible compared to shape effects, even at the scale of microrobots.

In [49] the total force ${}^b\mathbf{F}_b$ and torque ${}^b\mathbf{T}_b$ on an assembled-MEMS microrobot is computed as the sum of the individual forces and torques on assembled parts. This is achieved by neglecting the magnetic interaction between the individual pieces, and by considering the microrobot as a superposition of simpler geometries as shown in Fig. 13.9, rather than using the actual complex shapes of the parts.

13.3.1 Magnetic Control in Fluids

Microrobots, like microorganisms, operate in a low-Reynolds-number regime. When controlling a magnetic object through Newtonian fluid at low-Reynolds-number

regime, the object nearly instantaneously reaches its terminal velocity \mathbf{V} where the viscous drag force, which is linearly related to velocity through a drag coefficient ψ_v , exactly balances the applied magnetic force \mathbf{F} :

$$\mathbf{F} = \psi_v \mathbf{V} \quad (13.11)$$

Similarly, the object nearly instantaneously reaches its terminal rotational velocity Ω where the viscous drag torque, which is linearly related to rotational velocity through a drag coefficient ψ_ω , exactly balances the applied magnetic torque \mathbf{T} .

$$\mathbf{T} = \psi_\omega \Omega \quad (13.12)$$

If we consider a spherical body of diameter d and a fluid with viscosity η , the translational and rotational drag coefficients are described in Stokes flow (see [64]) as:

$$\psi_v = 3\pi\eta d \quad (13.13)$$

$$\psi_\omega = \pi\eta d^3 \quad (13.14)$$

It is clear that velocity is inversely proportional to fluid viscosity with all other parameters held constant.

In [39] hydrodynamic properties of assembled-MEMS microrobots are determined experimentally by placing a microrobot in a known-fluid-filled vial and tracking it by digital cameras as it sinks under its own weight and under different applied magnetic forces. Modeling an assembled-MEMS microrobot as a sphere for the purposes of calculating fluid drag is found to be quite accurate. This also agrees with the typical assumption that fluid drag is insensitive to geometry at low Reynolds number. The coefficient of viscous drag of the microrobot in a Newtonian fluid obtained in [39] is found to be $\psi_v = (1.41 \times 10^{-2} \text{N} \cdot \text{s/m}) \cdot d$.

The calculations in this section assume a Newtonian fluid, which will be a valid assumption after a vitrectomy has been performed. In the presence of intact vitreous humor, a more complicated fluid model must be considered.

13.3.2 *Developing Sufficient Force for Levitation and Puncture*

There is interest in determining the amount of force that can be developed wirelessly for the purpose of puncturing retinal veins. A drug delivery method where the microrobot docks to a blood vessel to allow the drug to release over extended periods of time is proposed, as shown in Fig. 13.10. This will require a microneedle to puncture the blood vessel. The magnetic forces on microrobots in applied magnetic fields are well understood. However, the magnitude of forces needed to puncture retinal veins is not available in the literature.



Fig. 13.10 Concept photo of a microrobot docked to a blood vessel for drug delivery (©IEEE 2008), reprinted with permission [17]. The assembled-MEMS microrobot shown is based on [66]

13.3.2.1 Retinal Puncture Forces

In [34], retinal puncture forces together with the scleral interaction forces are measured. However, needle and blood-vessel size, which affect puncture forces, are not specified. In [30], a retinal pick equipped with strain gauges is used to manipulate the retina of porcine cadaver eyes, and the range of forces acquired during a typical procedure is reported. However, the force of an individual retinal vein puncture is not provided. Conducting *in vivo* experiments on animal eyes is difficult with a high risk of tissue damage, and postmortem experiments may provide inaccurate results due to rapid changes in tissue properties of vessels after death. In [17], forces required for retinal vein punctures are measured and analyzed. Experimental data is collected from the vasculature of chorioallantoic membranes (CAM) of developing chicken embryos. The CAM of the developing chicken embryo has been used by ophthalmologists as a model system for studying photodynamic therapy and ocular angiogenesis. Recently, it was reported that the CAM of a twelve-day-old chicken embryo is a valid test bed for studies on human retinal vessel puncture [41]. The CAM's anatomical features and physiologic and histologic responses to manipulation and injury make it an effective living model of the retina and its vasculature. The vasculature of a twelve-day-old CAM and a human retina have roughly the same diameter and wall thickness (i.e., vessels with 100–300 μm outer diameter). The measurements are done using a capacitive force sensor with an attached microneedle, mounted on a 3-DOF Cartesian micromanipulator. Microneedles were pulled out of 1 mm OD boron-silicate glass pipettes in a repeatable way using a pipette puller and the outer diameters were inspected with a microscope.

There is variance in the force data due to effects that are not accounted for, such as anatomical variance between individual vessels and embryos, the state of the embryo (e.g., blood pressure, temperature), non-Hookean behavior of the vessel walls, errors in measured microneedle diameter, and error in the angle of incidence

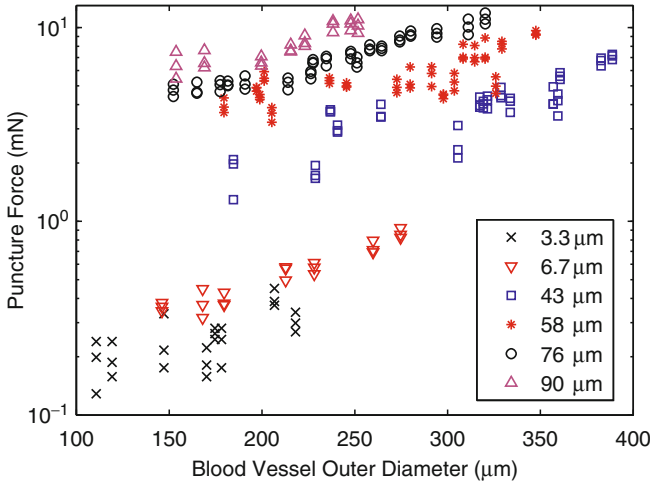


Fig. 13.11 Experimental data of puncture force with blunt tip microneedles vs. vessel diameter for different microneedles ODs (©IEEE 2008), reprinted with permission [17]

of the microneedle with respect to the blood vessel. Despite the variance, the data exhibit clear trends, as shown in Fig. 13.11. It is observed that there is an approximately quadratic trend in blood-vessel diameter and an approximately linear trend in microneedle diameter.

The experiments are performed with blunt-tip needles, so the forces shown in Fig. 13.11 should be taken as upper bounds for required puncture forces. It is known that beveling the needle's tip will significantly reduce the puncture forces [5, 16].

In [30], it is shown that 88% of all tool/tissue interaction forces during vitreoretinal surgery are below 12.5 mN, which corresponds well with the results shown in Fig. 13.11. In [34], higher puncture forces with larger variance than the results in Fig. 13.11 are reported. However, the reported forces include scleral interaction forces, and the force sensor is mounted on a handheld device.

13.3.2.2 Developing Sufficient Force

Let us consider a microrobot assembled from two thin elliptical pieces, as shown in the inset of Fig. 13.12. The volume of this microrobot is given by $v = 2\pi abt - 2a^2t^2$. The force on such assembled microrobots made of Ni and CoNi are measured using the magnetic measurement system described in [39], and the results are shown in Fig. 13.12. The system uses a 40 mm × 40 mm × 20 mm NdFeB magnet with the north and south poles on the largest faces, and a field value of 0.41 T measured in the center of the north pole face. In addition to the measured data, a microrobot made of permanent-magnetic (hard-magnetic) material with a remanence magnetization of 4×10^5 A/m, which is a value that can currently be achieved using microfabrication techniques, is simulated.

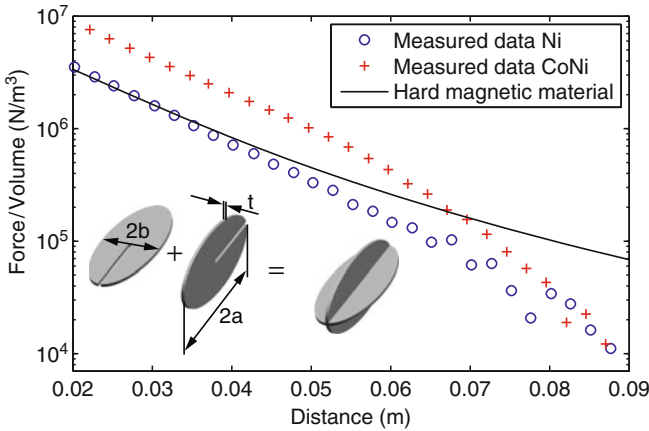


Fig. 13.12 Experimental data of normalized force vs. distance of the microrobot from the magnet's surface (©IEEE 2008), reprinted with permission. The magnet is described in [39]. A simulation of permanent-magnetic material with a remanence of 4×10^5 A/m is also shown. *Inset:* Definition of dimensions of the assembled microrobots used

In Fig. 13.12 we see that magnetic force drops off rapidly with increasing distance between the microrobot and the magnet. Increasing the saturation magnetization of a soft-magnetic material (compare CoNi and Ni) can lead to increases in force in a high-field region. Even relatively poor soft-magnetic materials (Ni) match good permanent magnets in a high-field region since the saturation magnetization values for soft-magnetic materials are typically higher than the remanence magnetization values of permanent magnets. However, as field strength is reduced, and the soft-magnetic microrobots are no longer saturated, they begin to provide similar force, and each provides less than that of the permanent-magnetic material. This is due to the magnetization of the soft-magnetic material, which is a function of the applied field, dropping below the remanence of the permanent-magnetic material.

Let us consider a microrobot with dimensions $a = 1000 \mu\text{m}$, $b = 500 \mu\text{m}$, and $t = 100 \mu\text{m}$, and a volume of $v = 3 \times 10^{-10} \text{m}^3$; this microrobot could be electroplated and assembled, and fit through a 1-mm incision. If we consider the microrobot at a position 70 mm away from the surface of the magnet, soft- and permanent-magnet materials provide approximately the same force of 0.05 mN. For a length comparison, the diameter of the human eye is 25 mm, so this places the surface of the magnet almost three eye diameters away from the microrobot. If we move the microrobot only about 10 mm closer to the magnet, we gain an order of magnitude in our magnetic force, bringing it beyond the level needed for puncturing retinal veins with a blunt-tip needle of a few micrometers in size. As mentioned previously, beveling the needle's tip would reduce the required force even further. The magnet used in the experiment was chosen somewhat arbitrarily; other magnet shapes and sizes can be chosen to project the magnetic field at greater distances.

Under the above considerations, it seems feasible that enough magnetic force can be developed by pulling with magnetic field gradients to puncture retinal veins,

provided that the microneedle is made small enough and sharp enough. These demands are attainable with current microfabrication technology. Puncture also requires an intelligent design of the magnetic-field generation system, which will use the superimposed fields of multiple permanent magnets or electromagnets, increasing the ability to generate strong fields at a distance. The choice of soft- or permanent-magnetic material for the microrobot will ultimately depend on the design of the magnetic-field generation system. This issue of force generation is discussed further in the next section.

It has been shown that microrobots that swim using helical propellers that mimic bacterial flagella theoretically have the potential to develop higher forces than obtained with gradient-based force generation at small scales [4]. It has also recently been shown that magnetic helical microrobots can be fabricated and wirelessly controlled [67]. This provides another option for retinal drug delivery.

13.3.3 *OctoMag*

There are two viable sources for the generation of controlled magnetic fields: permanent magnets and electromagnets. Permanent magnets exhibit a very advantageous volume to field-strength ratio. However, if we are interested in medical applications, electromagnets offer simpler real-time control, and present an inherently safer choice. A system using electromagnets can be implemented such that no moving parts are required to control magnetic field strength. This is important for both patient and medical-personnel safety. In addition, electromagnets are safer in the event of system failure: permanent magnets retain their attractive/repulsive strength in case of sudden power loss, whereas an electromagnetic system becomes inert, and in addition for the case of an intraocular microrobotic agent, the microrobot would slowly drift down under its own weight rather than experiencing uncontrolled forces with the potential of inflicting irreparable damage inside the eye. Using an array of stationary magnetic field sources also simplifies the task of designing a system that will respect the geometry of the human head, neck, and shoulders.

Bearing these considerations in mind, a robotic system called OctoMag for 5-DOF wireless magnetic control of a fully untethered microrobot (3-DOF position, 2-DOF pointing orientation) was developed at ETH Zurich [38]. It is difficult to control torque about the axis of \mathbf{M} using the simple model in (7), which is why 5-DOF control was achieved as opposed to 6-DOF control. A concept image of how the system would be used for the control of intraocular microrobots can be seen in Fig. 13.13.

13.3.3.1 Control with Stationary Electromagnets

Soft-magnetic-core electromagnets can create a magnetic field that is approximately 20 times stronger than the magnetic field created by air-core electromagnets, for the geometry shown in Fig. 13.13. As opposed to air-core electromagnets, their

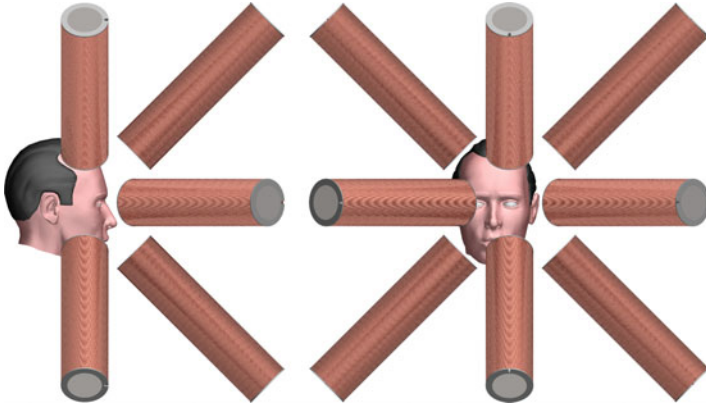


Fig. 13.13 Concept image of the OctoMag electromagnetic system: An eyeball is at the center of the system's workspace (©IEEE 2010), reprinted with permission. The electromagnet arrangement accommodates the geometry of the head, neck, and shoulders. The OctoMag is designed for a camera to fit down the central axis to image the microrobot in the eye

individual magnetic fields are coupled, which complicates modeling and control. However, cores made of high-performance soft-magnetic materials impose only a very minor constraint on modeling and control [38].

Within a given static arrangement of electromagnets, each electromagnet creates a magnetic field throughout the workspace that can be precomputed. At any given point in the workspace \mathbf{P} , the magnetic field due to a given electromagnet can be expressed by the vector $\mathbf{B}_e(\mathbf{P})$, whose magnitude varies linearly with the current through the electromagnet, and as such can be described as a unit-current vector in units T/m multiplied by a scalar current value in units A:

$$\mathbf{B}_e(\mathbf{P}) = \tilde{\mathbf{B}}_e(\mathbf{P})i_e \quad (13.15)$$

The subscript e represents the contribution due to the e^{th} electromagnet. However, although the field $\mathbf{B}_e(\mathbf{P})$ is the field due to the current flowing through only electromagnet e , it is due to the soft-magnetic cores of every electromagnet. With air-core electromagnets, the individual field contributions are decoupled, and the fields can be individually precomputed and then linearly superimposed. This is not the case with soft-magnetic-core electromagnets. However, if an ideal soft-magnetic material with negligible hysteresis is assumed, and the system is operated with the cores in their linear magnetization region, the assumption is still valid that the field contributions of the individual currents (each of which affect the magnetization of every core) superimpose linearly. Thus, if the field contribution of a given electromagnet is precomputed in situ, it can be assumed that the magnetic field at a point in the workspace is the sum of the contributions of the individual currents. This assumption is clearly also valid for air-core electromagnets and the linear summation of fields can be expressed as:

$$\mathbf{B}(\mathbf{P}) = [\tilde{\mathbf{B}}_1(\mathbf{P}) \cdots \tilde{\mathbf{B}}_n(\mathbf{P})] \begin{bmatrix} i_1 \\ \vdots \\ i_n \end{bmatrix} = \mathcal{B}(\mathbf{P})\mathbf{I} \quad (13.16)$$

The $3 \times n$ $\mathcal{B}(\mathbf{P})$ matrix is defined at each point \mathbf{P} in the workspace, which can either be analytically calculated online, or a grid of precomputed or measured points can be interpolated online. It is also possible to express the derivative of the field in a given direction in a specific frame, for example the x direction, as the contributions from each of the currents:

$$\partial \mathbf{B}(\mathbf{P}) \partial x = \left[\frac{\partial \tilde{\mathbf{B}}_1(\mathbf{P})}{\partial x} \cdots \frac{\partial \tilde{\mathbf{B}}_n(\mathbf{P})}{\partial x} \right] \begin{bmatrix} i_1 \\ \vdots \\ i_n \end{bmatrix} = \mathcal{B}_x(\mathbf{P})\mathbf{I} \quad (13.17)$$

If we are interested in controlling a microrobot moving through fluid, where the microrobot can align with the applied field unimpeded, rather than controlling torque and force acting on the microrobot, we can simply control the magnetic field to the desired orientation, to which the microrobot will naturally align, and then explicitly control the force on the microrobot:

$$\begin{bmatrix} \mathbf{B} \\ \mathbf{F} \end{bmatrix} = v \begin{bmatrix} \mathcal{B}(\mathbf{P}) \\ \mathbf{M}^T \mathcal{B}_x(\mathbf{P}) \\ \mathbf{M}^T \mathcal{B}_y(\mathbf{P}) \\ \mathbf{M}^T \mathcal{B}_z(\mathbf{P}) \end{bmatrix} \begin{bmatrix} i_1 \\ \vdots \\ i_n \end{bmatrix} = \mathcal{A}(\mathbf{M}, \mathbf{P})\mathbf{I} \quad (13.18)$$

That is, for each microrobot pose, the n electromagnet currents are mapped to a field and force through a $6 \times n$ actuation matrix $\mathcal{A}(\mathbf{M}, \mathbf{P})$. For a desired field/force vector, the choice of currents that gets us closest to the desired field/force value can be found using the pseudoinverse:

$$\mathbf{I} = \mathcal{A}(\mathbf{M}, \mathbf{P})^\dagger \begin{bmatrix} \mathbf{B}_{des} \\ \mathbf{F}_{des} \end{bmatrix} \quad (13.19)$$

Full 5-DOF control requires a rank-6 actuation matrix \mathcal{A} . If there are multiple solutions to achieve the desired field/force, the pseudoinverse finds the solution that minimizes the 2-norm of the current vector, which is desirable for the minimization of both power consumption and heat generation. Note that the use of (19) requires knowledge of the microrobot's pose and magnetization. If the direction of \mathbf{B} does not change too rapidly, it is reasonable to assume that \mathbf{M} is always aligned with \mathbf{B} ,

which means that one need not explicitly measure the microrobot's full pose, but rather, must only estimate the magnitude of \mathbf{M} and measure the microrobot's position \mathbf{P} . In addition, if the magnetic field does not vary greatly across the workspace, it may be reasonable to assume that the microrobot is always located at $\mathbf{P} = \mathbf{0}$ for purposes of control, eliminating the need for any localization of the microrobot.

There are a number of potential methods to generate the unit-current field maps that are required for the proposed control system. One can either explicitly measure the magnetic field of the final system at a grid of points or compute the field values at the grid of points using FEM models. In either case trilinear interpolation is used during real-time control. To generate the unit-current gradient maps using either method, one can either explicitly measure/model the gradient at the grid of points, or numerically differentiate the field data. Alternatively, one can fit an analytical model – for example the point-dipole model [24] – to field data obtained from an FEM model of the final system for each of the unit-current contributions. An analytical field model also has an analytical derivative. These analytical models can then be used to build the unit-current field and gradient maps during run time.

13.3.3.2 System Implementation

Equipped with a general control system using n stationary electromagnets, it is now possible to use this controller in the design of a suitable electromagnet configuration. The singular values of the actuation matrix in (18) provide information on the condition of the workspace and can be used as performance metric in a design optimization [38]. Figure 13.14 shows a physical embodiment of the concept image presented earlier. This prototype setup was designed with a workspace that is large enough that, after experimenting in artificial and ex vivo eyes, could be used for animal trials with live cats and rabbits.

Each electromagnet is completely filled with a core made of VACOFLUX 50 – a CoFe alloy from VACUUMSCHMELZE – with a diameter of 42 mm. This material has a saturation magnetization on the order of 2.3 T, a coercivity of 0.11 mT, and a maximum permeability of 4500 H/m. To prevent temperatures inside the coils to elevate beyond 45°C, every electromagnet is wrapped with a cooling system. The current for the electromagnetic coils is sourced through custom-designed switched amplifiers to reduce the power consumption. Two stationary camera assemblies provide visual feedback from the top and side and allow to extract the 3-D position of a microrobot in the system. For the envisioned intraocular application the visual feedback will have to be produced using a single camera which is detailed in Sect. 4.

An example of the manipulation capabilities of the system can be seen in Fig. 13.15. Automated pose control refers to closed-loop position control with open-loop orientation control. The system exhibits similar performance in a wide array of different trajectories as well as for a variety of robot orientations. The forces this

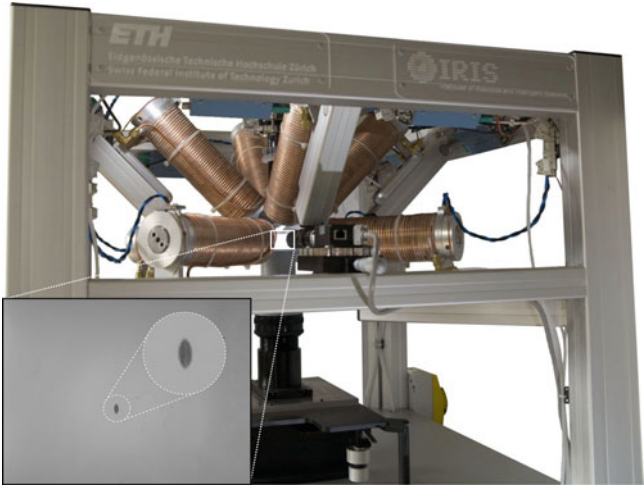


Fig. 13.14 OctoMag prototype: The system contains eight 210-mm-long by 62-mm-diameter electromagnets (©IEEE 2010), reprinted with permission. The gap between two opposing electromagnets on the lower set is 130 mm. The inset shows a 500- μ m-long microrobot of the type described in [66] levitating in a chamber. This is the side-camera view seen by the operator

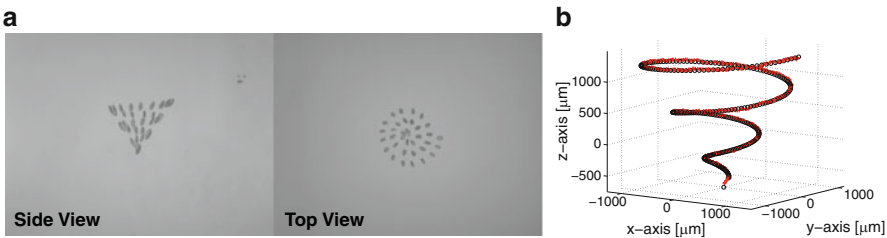


Fig. 13.15 Demonstration of automated pose control (©IEEE 2010), reprinted with permission. Both time-lapse image sequences (a) show a 500- μ m-long microrobot following a spiral trajectory keeping its orientation constantly pointing at the vertex of the spiral. Way points (*black circle*) and tracker data (*red plus*) are shown in the isometric graph (b). Average trajectory-completion time: 33.4 s

system can exert on the tiny Ni microrobot shown in Figs. 13.14 and 13.15 as well as on a larger NdFeB cylinder with a diameter of 500 μ m and a height of 1 mm are tabulated in Table 13.1.

13.4 Issues in Localizing Microrobots

In the previous sections, we have discussed the functionalization of the microdevices and the principles of their control. In order to control these devices near the retina, knowledge of their position is usually required. In the case of untethered magnetic

Table 13.1 Maximum force in OctoMag setup on a small Ni microrobot and a full NdFeB cylinder for various agent orientations (©IEEE 2010), reprinted with permission

Field Orientation	Ni Microrobot					NdFeB Cylinder				
	F_{up} (μN)	F_{down} (μN)	$F_{lat,x}$ (μN)	$F_{lat,y}$ (μN)	$F_{lat,xy}$ (μN)	F_{up} (μN)	F_{down} (μN)	$F_{lat,x}$ (μN)	$F_{lat,y}$ (μN)	$F_{lat,xy}$ (μN)
z	2.1	1.3	1.1	1.3	1.4	281	221	141	172	200
$-z$	3.3	2.1	1.7	2.0	2.2	281	221	141	172	200
x	2.2	2.2	3.6	3.1	3.9	189	222	213	341	276
xy	2.7	2.7	4.1	3.0	2.5	274	263	263	286	259

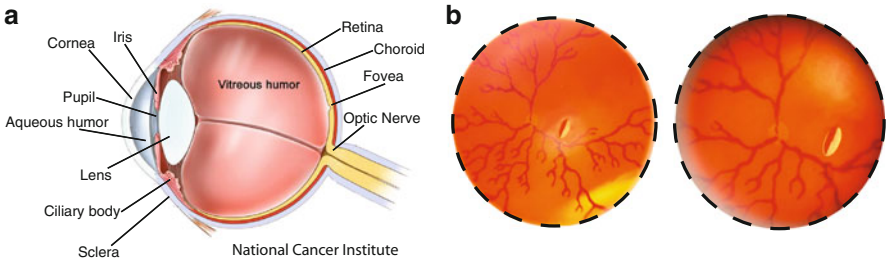


Fig. 13.16 (a) Anatomy of the human eye. (b) The biomedical microrobot of [66] in the model eye [31]. *The left image* shows the intraocular environment without the eye’s optical elements, and *the right image* shows the effect of the model eye optics. Images are taken with an unmodified digital camera (©IEEE 2008), reprinted with permission

devices, knowledge of the position of the device within the magnetic field is necessary for precise control [2, 49]. Since, the interior of the human eye is externally observable, vision can be used to perform 3D localization. In addition, with clear images of the retina and the microrobot, visual feedback can be used to close a visual-servoing loop to correct for any errors in the localization procedure.

Ophthalmic observation has been practices for centuries, with its most critical task being to be able to visualize the human retina with high-definition. Nowadays, clinicians have the ability to acquire magnified images of the human retina using an ever-increasing variety of optical tools that are designed specifically for the unique optical system that is the human eye (Fig. 13.16).

However, keeping intraocular objects that are freely moving in the vitreous humor of the eye (and not just on the retina) constantly in focus is challenging, and the captured images are often blurry and noisy. The unstructured illumination that reaches the interior of the eye, either through endoillumination, transpupillary or transscleral means, can deteriorate the images with uneven brightness and backreflections. Moreover, the microtools that operate in the human eye are generally specular, and have no distinctive color features. For precise localization, robust visual tracking that detect the microrobot in the images is needed. The extracted segmentation information will be used for 3D localization.

The literature lacks algorithms for the localization of untethered intraocular devices. In addition, because the microrobots will be controlled by a magnetic-field-generation system surrounding the patient's head, we are interested in compact solutions that utilize a single stationary camera. In the following sections, we will introduce the first intraocular localization algorithm, using a custom-built stationary camera. Our approach is based on depth-from-focus [20]. Focus-based methods do not require a model of the object of interest, but only knowledge of the optical system. Applied in the eye, they could also localize unknown objects such as floaters. As a result, our analysis need not be considered only in the scope of microrobot localization, but is applicable on any type of unknown foreign bodies.

In the following, we will firstly evaluate different ophthalmoscopy methods with respect to their advantages in imaging and localizing. Then, based on our results, we will introduce a level-set tracking algorithm that successfully segments intraocular microdevices in images. Finally, we will present a method for wide-angle intraocular localization.

13.4.1 Comparison of Ophthalmoscopy Methods

Our results are based on Navarro's schematic eye [22] (i.e. an optical model based on biometric data that explains the optical properties of the human eye). Navarro's schematic eye performs well for angles up to 70° measured from the center of the pupil and around the optical axis. For greater angles, the biometric data of each patient should be considered individually. Simulations are carried out with the OSLO optical lens design software. Throughout this section, the object's depth z is measured along the optical axis. We begin by investigating the feasibility of imaging and localizing intraocular devices using existing ophthalmoscopy methods.

13.4.1.1 Direct Ophthalmoscopy

In a relaxed state, the retina is projected through the eye optics as a virtual image at infinity. An imaging system can capture the parallel beams to create an image of the retina. In direct ophthalmoscopy the rays are brought in focus on the observer's retina [57]. By manipulating the formulas of [56] the field-of-view for direct ophthalmoscopy is found as 10° (Fig. 13.17a).

Every object inside the eye creates a virtual image. These images approach infinity rapidly as the object approaches the retina. Figure 13.18 (solid line) displays the distance where the virtual image is formed versus different positions of an intraocular object. In order to capture the virtual images that are created from objects close to the retina, an imaging system with near to infinite working distance is required. Such an imaging system will also have a large depth-of-field, and depth information from focus would be insensitive to object position (Table 13.2).

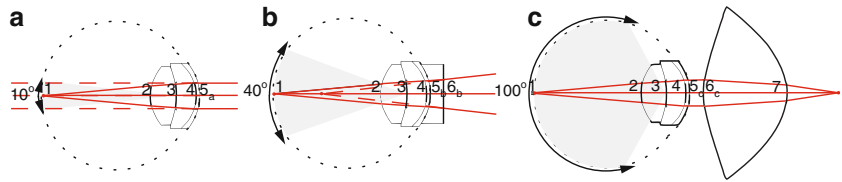


Fig. 13.17 (a) Direct ophthalmoscopy with Navarro’s schematic eye [22]. (b) Ophthalmoscopy with Navarro’s schematic eye with a vitrectomy lens [23]. (c) Indirect ophthalmoscopy with Navarro’s schematic eye with a condensing lens [63] (©IEEE 2008), reprinted with permission

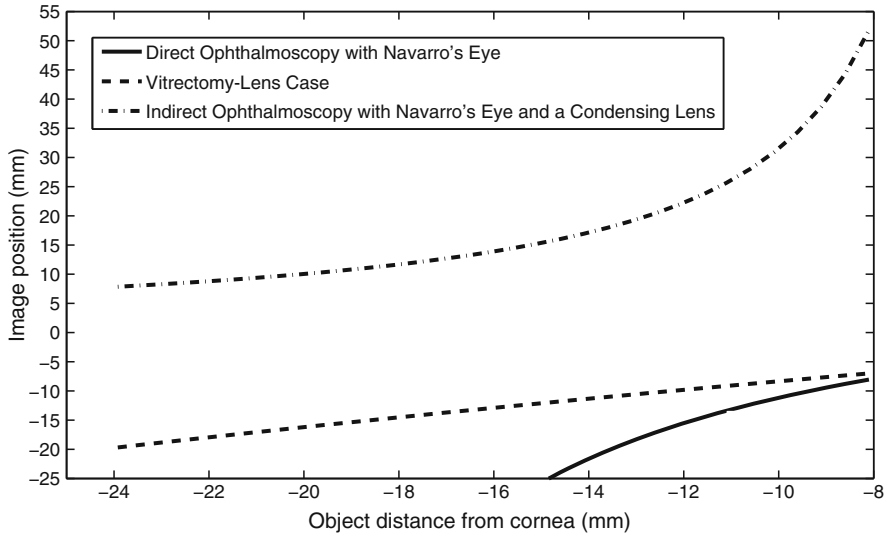


Fig. 13.18 Image position versus intraocular object position for the direct ophthalmoscopy case, the vitrectomy-lens case, and the indirect ophthalmoscopy case. Image distances are measured from the final surface of each optical system (5a, 6b, 7 respectively) (©IEEE 2009), reprinted with permission

13.4.1.2 Vitrectomy Lenses

To visualize devices operating in the vitreous humor of phakic (i.e. intact intraocular lens) eyes, only plano-concave lenses (Fig. 13.17b) need to be considered [57]. Vitrectomy lenses cause the virtual images of intraocular objects to form inside the eye, allowing the imaging systems to have a reduced working distance. Based on data given from HUCO Vision SA for the vitrectomy lens S5.7010 [23], we simulated the effects of a plano-concave vitrectomy lens on Navarro’s eye (Fig. 13.17b). This lens allows for a field-of-view of 40°, significantly larger than the one obtainable with the method described in Sect. 4.1.1.

As shown in Fig. 13.18 (dashed line), the virtual images are formed inside the eye and span a lesser distance. Thus, contrary to direct observation, imaging with an

Table 13.2 Optical parameters for the systems of Fig. 13.17 (© IEEE 2008), reprinted with permission

Surface	1	2	3	4	5a	5b	5c	6b	6c	7
Radius (mm)	12.00	6.00	-10.20	-6.50	-7.72	-7.72	-7.72	∞	11.65	-9.48
Conic constant	0.00	-1.00	-3.13	0.00	-0.26	-0.26	-0.26	0.00	-9.24	-1.07
Thickness (mm)	16.32	4.00	3.05	0.55	∞	2.00	2.00	∞	13.00	∞
Refraction index	1.336	1.420	1.337	1.376	1.000	1.425	1.000	1.000	1.523	1.000

optical microscope (relatively short working distance and depth-of-field) is possible. The working distance of such a system must be at least 20 mm. As depth-of-field is proportional to working distance, there is a fundamental limit to the depth-from-focus resolution achievable with vitrectomy lenses.

13.4.1.3 Indirect Ophthalmoscopy

Indirect ophthalmoscopy (Fig. 13.17c) allows for a wider field of the retina to be observed. A condensing lens is placed in front of the patient's eye, and catches rays emanating from a large retinal area. These rays are focused after the lens, creating an aerial image of the patient's retina. Condensing lenses compensate for the refractive effects of the eye, and create focused retinal images.

We simulated the effects of a double aspheric condensing lens based on information found in [63]. This lens, when placed 5 mm from the pupil, allows imaging of the peripheral retina and offers a field-of-view of 100° . As a result, it can be part of an imaging system with a superior field-of-view than the ones described in Sect. 4.1.1 and Sect. 4.1.2. The image positions versus the intraocular object positions can be seen in Fig. 13.18 (dashed-dotted line). A sensing system with a short working-distance and shallow depth-of-field can be used in order to extract depth information from focus for all areas inside the human eye. Depth estimation is more sensitive for objects near the intraocular lens, since smaller object displacements result in larger required focusing motions.

Dense CMOS sensors have a shallow depth-of-focus, and as a result, they can be used effectively in depth-from-focus techniques. Based on Fig. 13.18, to localize objects in the posterior of the eye a sensor travel of 10 mm is necessary. A $24 \times 24 \text{ mm}^2$ CMOS sensor can capture the full field-of-view. The simulated condensing lens causes a magnification of 0.78×9 and thus, a structure of $100 \mu\text{m}$ on or near the retina will create an image of $78 \mu\text{m}$. Even with no additional magnification, a CMOS sensor with a common sensing element size of $6 \times 6 \mu\text{m}^2$ will resolve small retinal structures sufficiently. As a conclusion, direct sensing of the aerial image leads to a high field-of-view, while having advantages in focus-based localization.

In the following, we will use indirect ophthalmoscopy methods for tracking and localizing intraocular microrobots.

13.4.2 Tracking Intraocular Microrobots

To track intraocular microrobots, we use the method presented in [10], which is based on the framework developed in [54]. For successful tracking to occur, one should evaluate the quality of different colorspace with respect to the biomedical application of interest. For example, in [18, 7, 61] the Hue-Saturation-Value (HSV) colorspace is used, but in [10] it is shown that this is a not suitable colorspace in

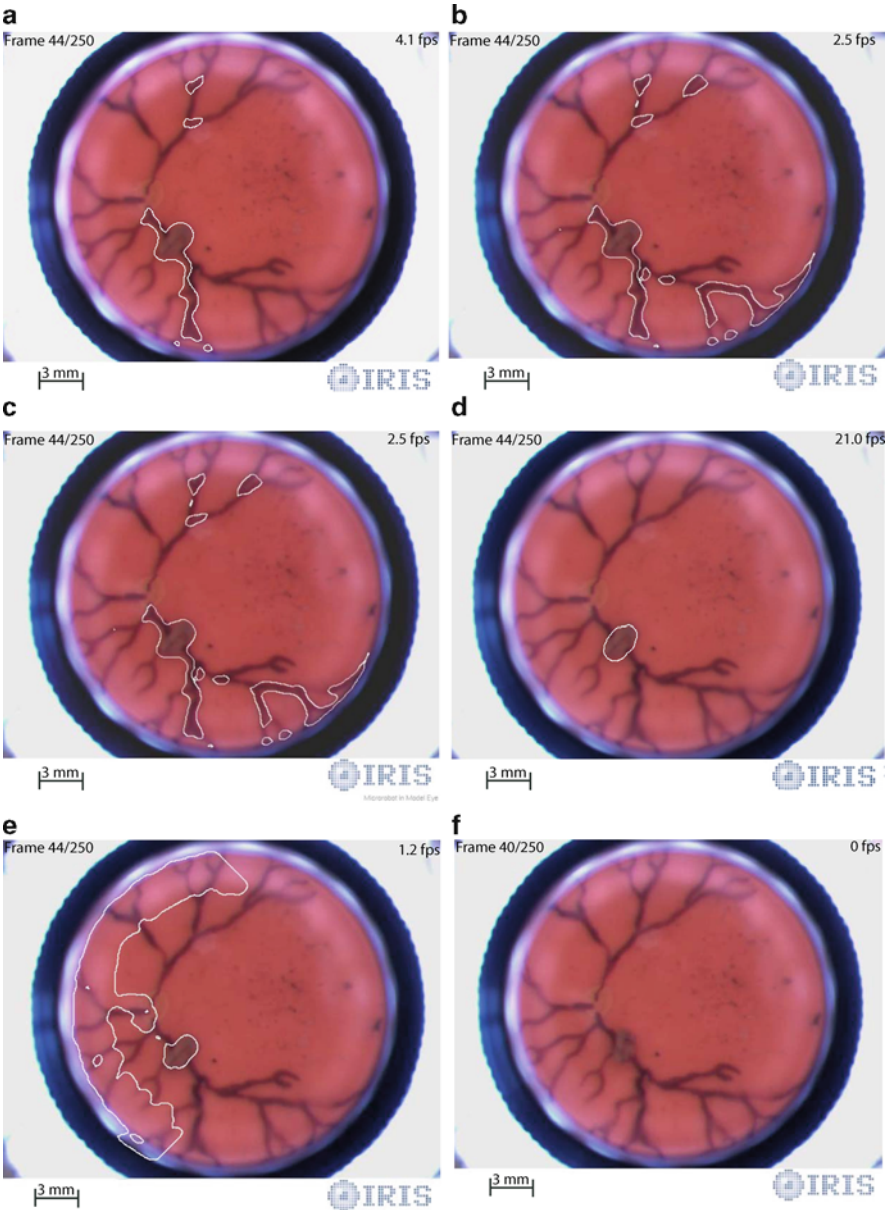


Fig. 13.19 Tracking using (a), (b) the R-G channels of the RGB colorspace without and with thresholds, respectively, (c), (d) the Y-V channels of the YUV colorspace without and with thresholds, respectively, (e), (f) the H-S channels of the HSV colorspace without and with thresholds, respectively (© IEEE 2009), reprinted with permission

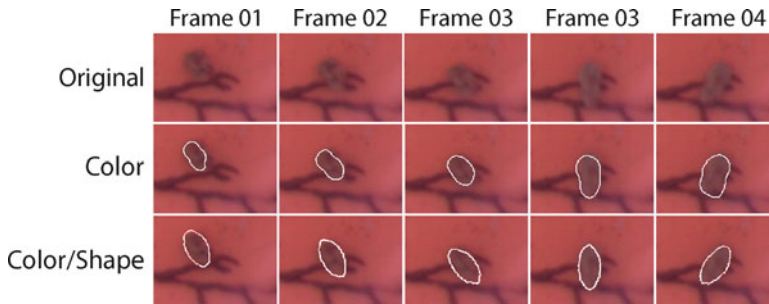


Fig. 13.20 Tracking using color information and color/shape information, for different frame sequences (©IEEE 2009), reprinted with permission

which to track intraocular microdevices. Tracking in the best colorspace ensures reduced vein segmentation; compare Fig. 13.19a with Fig. 13.19c and Fig. 13.19e).

After choosing the appropriate colorspace, thresholds that ensure the maximum object-from-background separation are calculated. These thresholds help vanish the erroneous vein segmentation, and lead to successful detection of the microrobot in the images (Fig. 13.19b, d). If the selected colorspace/channel combination is not of appropriate quality, the thresholds will cause the tracking to fail (Fig. 13.19e).

To further increase the segmentation accuracy, in [10], the statistical shape prior evolution framework of [42] is adapted and used. Using shape information together with the color information ensures diminished vein segmentation, as the misclassifications are discarded by the shape information. Figure 13.20 compares tracking in R-G, and tracking in R-G using shape information; when shape information is incorporated the results are improved.

13.4.3 Wide-Angle Localization

With the tracking method of [10] we can robustly estimate the position of an intraocular microrobot in images, successfully handling cases of occlusion and of defocus. However, in order to perform accurate magnetic control, we need to know its 3D position in the intraocular environment. Here, we present a method for wide-angle intraocular localization using focus information. This method was first introduced by Bergeles *et al.* [12].

13.4.3.1 Theory of Intraocular Localization

As previously stated, the condensing lens projects the spherical surface of the retina onto a flat aerial image. Moving the sensor with respect to the condensing lens focuses the image at different surfaces inside the eye, which we call *isofocus*

The isopixel curves are lines, and it is straightforward to parametrize them using their slope and their distance from the optical axis at the pupil. Each isopixel curve corresponds to one pixel on the image, and its parameters are functions of the pixel's offset (measured from the image center) due to the rotational symmetry of the system. For the 2D case, two parameters are required.

In Fig. 13.22a–d the parametrizing functions of the isofocus surfaces and isopixel curves are displayed. The conic constant need not vary (fixed at -0.5) because it was observed that the surface variation can be successfully captured by the curvature. For each parameter, we fit the least-order polynomial that captures its variability. The parametrizing functions are injections (Fig. 13.22a–d), and thus, 3D intraocular localization with a wide-angle is unambiguous.

13.4.3.2 Localization Experiments

As an experimental testbed, we use the model eye [31] from Gwb International, Ltd. This eye is equipped with a plano-convex lens of 36 mm focal length that mimics the compound optical system of the human eye. Gwb International, Ltd. disclosed the lens' parameters so that we can perform our simulations. We also measured the model's retinal depth and shape.

The optical system under examination is composed of this model eye and the condensing lens of Fig. 13.17c, where the refraction index was chosen as 1.531. The simulated isofocus surfaces and isopixel curves of the composite system, together with their fits, are shown in Fig. 13.21b. Based on these simulations, we parametrize the isofocus surfaces and the isopixel curves (Fig. 13.22e–h). The behavior of the parameters is similar to the one displayed in Fig. 13.22a–d for Navarro's schematic eye. We assume an invariant conic constant of -1.05 , because the variability of the surfaces can be captured sufficiently by the curvature.

In order to calibrate the isofocus surfaces for their intersection with the optical axis, we perform an on-optical-axis depth-from-focus experiment on the aligned optical system. We use a Sutter linear micromanipulation stage to move a checkerboard calibration pattern in the model eye with 1 mm steps, and estimate the in-focus sensor position. The best focus position is estimated with techniques described in [58]. The estimated sensor positions with respect to different object depths can be seen in Fig. 13.23. The uncalibrated model fit is displayed with a solid line, and, as can be seen, calibration is needed.

In the model eye, we can calibrate for the relationship between the in-focus sensor position and the depth of the object using the full set of data points. However, such an approach would be clinically invasive as it would require a vitrectomy and a moving device inside the eye. The only minimally invasive biometric data available are the depth and shape of the retina that can be measured from MRI scans [8]. Assuming that there are accumulated errors that can be lumped and included as errors in the estimated image and object positions, it is shown in [11] that by using a first-order model of the optics, calibration using only the depth of the retina is possible. By adapting this method to our framework, we are able to

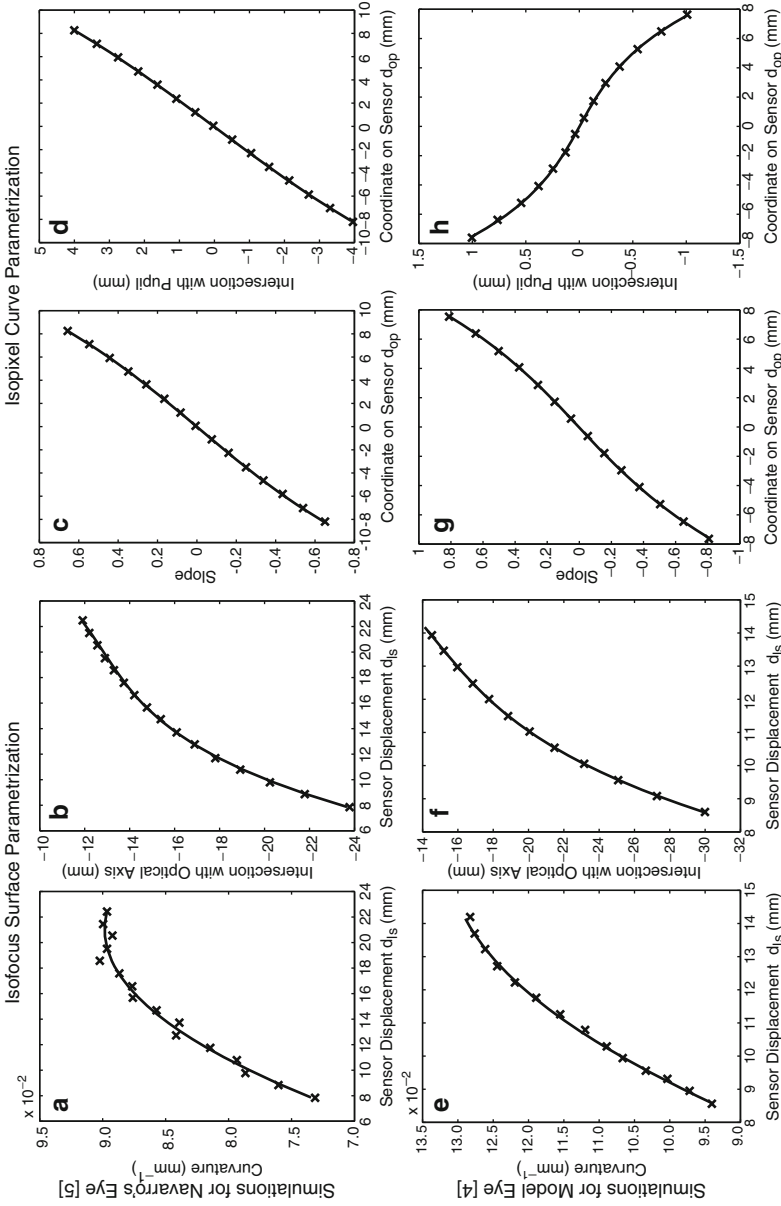


Fig. 13.22 *top row*: Parametrization polynomials for the system of Fig. 13.21a, and *bottom row*: for the system of Fig. 13.21b (©IEEE 2009), reprinted with permission. Isifocus surface parametrization: (a), (b), (e), (f) Fitted 2nd- and 3rd-order polynomials for the curvature and for the intersection with the optical axis. Isopixel curve parametrization: (c), (d), (g), (h) Fitted 3rd-order polynomials for the line slope and for the intersection with the pupil

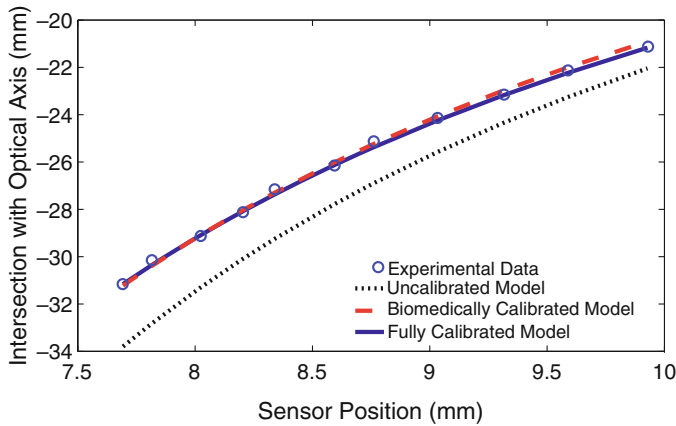


Fig. 13.23 Model fits for the function describing the intersection of the isofocus surfaces with the optical axis. Biometric calibration errors: mean = 159 μm , std = 94 μm (©IEEE 2009), reprinted with permission

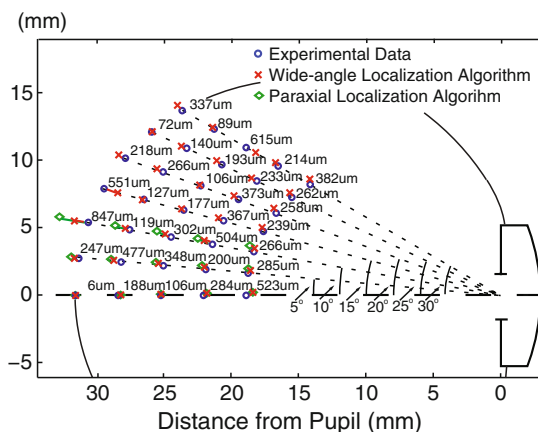
biometrically calibrate for the parameters of the polynomial that describes the intersection of the isofocus surfaces with the optical axis. The resulting fit can be seen in Fig. 13.23.

The remaining two parameters of the isofocus surfaces control the shape of the isofocus surfaces but not their position. The condensing lens is designed to create a flat aerial image of the retinal surface, and our experiments have shown that we can use it to capture an overall sharp image of the model eye's retina. Therefore, we conclude that there exists an isofocus surface that corresponds to the retinal surface, and we consider it as the first surface. From Fig. 13.21b we see that the first isofocus surface does indeed roughly correspond to the retinal shape (mean error = 371 μm). As a result, calibration for the conic constant and the curvature is not needed. If our model was not accurately predicting the shape of the retina, then we would calibrate the parameters of the first isofocus surface so that it has exactly the same shape as the retina.

To estimate the validity of the presented wide-angle localization algorithm, we consider points in the model eye for various angles with respect to the optical axis and various distances from the pupil. In Fig. 13.24, the results using the proposed wide-angle localization algorithm are displayed. For comparison, we also show the results based on the paraxial localization algorithm presented in [11] for angles up to 10° from the optical axis. The paraxial localization results deteriorate as the angles increase. However, the localization method proposed here can be used for regions away from the optical axis with high accuracy.

To fully control untethered devices, their position and orientation (i.e. their pose) must be estimated. Until now, we have only addressed position estimation. For the estimation of orientation, methods exist for perspective projection systems [19]. These methods work by projecting an estimate of the 6-DOF pose of a CAD model

Fig. 13.24 Localization experiment showing the validity of the proposed algorithm. Errors: mean = 282 μm , std = 173 μm (©IEEE 2009), reprinted with permission



of the device on the image, based on a calibrated camera projection matrix, and then adapting the estimate of the pose until projection agrees with the perceived image. It may be possible to apply similar methods for pose estimation of intraocular objects. However, the estimates of the pose would be projected on the image by making use of the isopixel curves. This topic is left as future work.

13.5 Conclusions

In this chapter we considered three topics in the design and control of intraocular microrobots. First, we discussed functional coatings – both for remote sensing and targeted drug delivery. We developed a wireless oxygen sensor, and we presented a method to deliver clot-busting tPA to retinal veins. Next, we discussed magnetic control. We showed that it is technically feasible to generate sufficient forces to puncture retinal veins. Finally, we showed that it is possible to visually track and then localize intraocular microrobots with a single stationary camera. The localization results can be utilized in the magnetic control system. The groundwork has been laid, and it won't be long before intraocular microrobots change the way that the most difficult retinal procedures are done.

Acknowledgments This research is supported by the NCCR Co-Me of the Swiss National Science Foundation. The authors would like to thank the many people that have contributed to this research: Berk Yeşin, Karl Vollmers, Zoltan Nagy, Brad Kratochvil, Ruedi Borer, Görkem Dogangil, Kamran Shamaei, and George Fagogenis, as well as Heike Hall from ETH Zurich, and Mohammad K. Nazeeruddin from Ecole Polytechnique Fédéral de Lausanne. The authors also would like to thank Justus Garweg, M.D. from the Swiss Eye Institute in Bern and Carsten Framme, M.D. of the Inselspital Bern for their guidance on vitreoretinal applications for untethered microrobots.

References

1. Stereotaxis (2007). URL <http://www.stereotaxis.com>
2. Abbott, J.J., Ergeneman, O., Kummer, M.P., Hirt, A.M., Nelson, B.J.: Modeling magnetic torque and force for controlled manipulation of soft-magnetic bodies. *IEEE Trans. Robot.* **23** (6), 1247–1252 (2007)
3. Abbott, J.J., Nagy, Z., Beyeler, F., Nelson, B.J.: Robotics in the small, part I: Microrobotics. *IEEE Robot. Automat. Mag.* **14**(2), 92–103 (2007)
4. Abbott, J.J., Peyer, K.E., Cosentino Lagomarsino, M., Zhang, L., Dong, L.X., Kaliakatsos, I.K., Nelson, B.J.: How should microrobots swim? *Int. J. Rob. Res.* **28**(11–12), 1434–1447 (2009)
5. Abolhassani, N., Patel, R., Moallem, M.: Needle insertion into soft tissue: A survey. *Med. Eng. Phys.* **29**, 413–431 (2007)
6. Amblard, F., Yurke, B., Pargellis, A., Leibler, S.: A magnetic manipulator for studying local rheology and micromechanical properties of biological systems. *Rev. Sci. Instrum.* **67**(3), 818–827 (1996)
7. Ascari, L., Bertocchi, U., Laschi, C., Stefanini, C., Starita, A., Dario, P.: A segmentation algorithm for a robotic micro-endoscope for exploration of the spinal cord. In: *IEEE Int. Conf. Robotics and Automation*, pp. 491–496 (2004)
8. Atchison, D.A., Pritchard, N., Schmid, K.L., Scott, D.H., Jones, C.E., Pope, J.M.: Shape of the retinal surface in emmetropia and myopia. *Invest. Ophthalmol. Vis. Sci.* **46**(8), 2698–2707 (2005)
9. Bach, M., Oschwald, M., Röver, J.: On the movement of an iron particle in a magnetic field. *Doc. Ophthalmol.* **68**, 389–394 (1988)
10. Bergeles, C., Fagogenis, G., Abbott, J.J., Nelson, B.J.: Tracking intraocular microdevices based on colorspace evaluation and statistical color/shape information. In: *Proc. IEEE Int. Conf. Robotics and Automation*, pp. 3934–3939 (2009)
11. Bergeles, C., Shamaei, K., Abbott, J.J., Nelson, B.J.: On imaging and localizing untethered intraocular devices with a stationary camera. In: *Proc. IEEE Int. Conf. on Biomedical Robotics and Biomechatronics* (2008)
12. Bergeles, C., Shamaei, K., Abbott, J.J., Nelson, B.J.: Wide-angle intraocular imaging and localization. In: *Int. Conf. Medical Image Computing and Computer Assisted Intervention*, vol. 1, pp. 540–548 (2009)
13. Bergeles, C., Shamaei, K., Abbott, J.J., Nelson, B.J.: Single-camera focus-based localization of intraocular devices. *IEEE Trans. Biomed. Eng.* **57**, 2064–2074 (2010)
14. Berkowitz, B., Wilson, C.: Quantitative mapping of ocular oxygenation using magnetic resonance imaging. *Magn. Reson. Med.* **33**(4), 579–581 (1995)
15. Cao, X., Lai, S., Lee, L.J.: Design of a self-regulated drug delivery device. *Biomed. Micro-devices* **3**(2), 109–118 (2001)
16. Davis, S.P., Landis, B.J., Adams, Z.H., Allen, M.G., Prausnitz, M.R.: Insertion of microneedles into skin: Measurement and prediction of insertion force and needle fracture force. *J. Biomech.* **37**, 1155–1163 (2004)
17. Dogangil, G., Ergeneman, O., Abbott, J.J., Pane, S., Hall, H., Muntwyler, S., Nelson, B.J.: Toward targeted retinal drug delivery with wireless magnetic microrobots. In: *Proc. IEEE/RSJ Int. Conf. on Intelligent Robots and Systems*, pp. 1921–1926 (2008)
18. Doignon, C., Graebling, P., de Mathelin, M.: Real-time segmentation of surgical instruments inside the abdominal cavity using a joint hue saturation color feature. *Real-Time Imaging* **11** (5–6), 429–442 (2005)
19. Drummond, T., Cipolla, R.: Real-time visual tracking of complex structures. *IEEE Trans. Pattern Anal. Mach. Intell.* **24**, 932–946 (2002)
20. Ens, J., Lawrence, P.: An investigation of methods for determining depth from focus. *IEEE Trans. Pattern Anal. Mach. Intell.* **15**(2), 97–108 (1993)

21. Ergeneman, O., Dogangil, G., Kummer, M.P., Abbott, J.J., Nazeeruddin, M.K., Nelson, B.J.: A magnetically controlled wireless optical oxygen sensor for intraocular measurements. *IEEE Sens. J.* **8**(1), 29–37 (2008)
22. Escudero-Sanz, I., Navarro, R.: Off-axis aberrations of a wide-angle schematic eye model. *J. Opt. Soc. A.* **16**(8), 1881–1891 (1999)
23. FCI Ophthalmics: (2009) S5.7010 planoconcave lens [Online]. Available: <http://www.fci-ophthalmics.com/html/retina.html#lenses>
24. Furlani, E.P.: Permanent Magnet and Electromechanical Devices. Academic Press, San Diego, California (2001)
25. Galloway, N.R., Amoaku, W.M.K., Galloway, P.H., Browning, A.C.: Common Eye Diseases and their Management, third edn. Springer, London (2005)
26. Geroski, D.H., Edelhauser, H.F.: Drug delivery for posterior segment eye disease. *Invest. Ophthalmol. Vis. Sci.* **41**(5), 961–964 (2000)
27. Ghazi, N.G., Noureddine, B.N., Haddad, R.S., Jurdi, F.A., Bashshur, Z.F.: Intravitreal tissue plasminogen activator in the management of central retinal vein occlusion. *Retina* **23**, 780–784 (2003)
28. Gillies, G.T., Ritter, R.C., Broadus, W.C., Grady, M.S., Howard, M.A. III, McNeil, R.G.: Magnetic manipulation instrumentation for medical physics research. *Rev. Sci. Instrum.* **65**(3), 533–562 (1994)
29. Grady, M.S., Howard, M.A. III, Molloy, J.A., Ritter, R.C., Quate, E.G., Gillies, G.T.: Nonlinear magnetic stereotaxis: Three-dimensional, in vivo remote magnetic manipulation of a small object in canine brain. *Med. Phys.* **17**(3), 405–415 (1990)
30. Gupta, P.K., Jensen, P.S., de Juan, E. Jr.: Surgical forces and tactile perception during retinal microsurgery. In: *Proc. Int. Conf. Med. Image Comput. and Comput.-Assisted Intervention*, pp. 1218–1225 (1999)
31. Gwb International, Ltd.: (2009) Model Eye (2mm pupil) [Online]. Available: http://www.gwbinternational.com/model_eye.htm
32. Ishiyama, K., Arai, K.I., Sendoh, M., Yamazaki, A.: Spiral-type micro-machine for medical applications. *J. Micromechatronics* **2**(1), 77–86 (2003)
33. Iwase, E., Shimoyama, I.: Multistep sequential batch assembly of three-dimensional ferromagnetic microstructures with elastic hinges. *J. Microelectromech. Syst.* **14**(6), 1265–1271 (2005)
34. Jagtap, A.D., Riviere, C.N.: Applied force during vitreoretinal microsurgery with handheld instruments. In: *Proc. IEEE Int. Conf. Engineering in Medicine and Biology Society*, pp. 2771–2773 (2004)
35. Jiles, D.: Introduction to Magnetism and Magnetic Materials. Chapman and Hall, London (1991)
36. Khamesee, M.B., Kato, N., Nomura, Y., Nakamura, T.: Design and control of a microrobotic system using magnetic levitation. *IEEE/ASME Trans. Mechatron.* **7**(1), 1–14 (2002)
37. Kirschkamp, T., Dunne, M., Barry, J.C.: Phakometric measurement of ocular surface radii of curvature, axial separations and alignment in relaxed and accommodated human eyes. *J. Ophth. Phys. Opt.* **24**(2), 65–73 (2004)
38. Kummer, M.P., Abbott, J.J., Kratochvil, B.E., Borer, R., Sengul, A., Nelson, B.J.: OctoMag: An electromagnetic system for 5-DOF wireless micromanipulation. In: *Proceedings of the International Conference on Robotics and Automation* (2010)
39. Kummer, M.P., Abbott, J.J., Vollmers, K., Nelson, B.J.: Measuring the magnetic and hydrodynamic properties of assembled-MEMS microrobots. In: *Proc. IEEE Int. Conf. Robotics and Automation*, pp. 1122–1127 (2007)
40. Lakowicz, J.R.: Principles of Fluorescence Spectroscopy, 2nd edn. Kluwer Academic/Plenum Publishers (1999)
41. Leng, T., Miller, J.M., Bilbao, K.V., Palanker, D.V., Huie, P., Blumenkranz, M.S.: The chick chorioallantoic membrane as a model tissue for surgical retinal research and simulation. *Retina* **24**(3), 427–434 (2004)

42. Leventon, M.E., Grimson, W.E.L., Faugeras, O.: Statistical shape influence in geodesic active contours. *IEEE Int. Conf. Computer Vision and Pattern Recognition* **1** (2000)
43. M. K. Tameesh *et al.*: Retinal vein cannulation with prolonged infusion of tissue plasminogen activator (t-PA) for the treatment of experimental retinal vein occlusion in dogs. *Am. J. Ophthalmol.* **138**(5), 829–839 (2004)
44. Mathieu, J.B., Beaudoin, G., Martel, S.: Method of propulsion of a ferromagnetic core in the cardiovascular system through magnetic gradients generated by an MRI system. *IEEE Trans. Biomed. Eng.* **53**(2), 292–299 (2006)
45. Meeker, D.C., Maslen, E.H., Ritter, R.C., Creighton, F.M.: Optimal realization of arbitrary forces in a magnetic stereotaxis system. *IEEE Trans. on Magnetics* **32**(2), 320–328 (1996)
46. Mejia-Barbosa, Y., Malacara-Hernandez, D.: A review of methods for measuring corneal topography. *J. Opt. Vis. Sci.* **78**(4), 240–253 (2001)
47. Mitchell, B., Koo, J., Iordachita, I., Kazanzides, P., Kapoor, A., Handa, J., Hager, G., Taylor, R.: Development and application of a new steady-hand manipulator for retinal surgery. In: *Proc. IEEE Int. Conf. Robotics and Automation*, pp. 623–629 (2007)
48. Mitra, A.K.: *Ophthalmic Drug Delivery Systems*. Marcel Dekker Inc., New York (2003)
49. Nagy, Z., Ergeneman, O., Abbott, J.J., Hutter, M., Hirt, A.M., Nelson, B.J.: Modeling assembled-MEMS microrobots for wireless magnetic control. In: *Proc. IEEE Int. Conf. Robotics and Automation*, pp. 874–879 (2008)
50. Park, J.H., Allen, M.G., Prausnitz, M.R.: Polymer microneedles for controlled-release drug delivery. *Pharm. Res.* **23**(5), 1008–1018 (2006)
51. Ratner, B.D., Hoffman, A.S., Schoen, F.J., Lemons, J.E. (eds.): *Biomaterials Science: An Introduction to Materials in Medicine*, second edn. Elsevier Academic Press (2004)
52. Riviere, C.N., Ang, W.T., Khosla, P.K.: Toward active tremor canceling in handheld microsurgical instruments. *IEEE Trans. on Robotics and Automation* **19**(5), 793–800 (2003)
53. Shahid, H., Hossain, P., Amoaku, W.M.: The management of retinal vein occlusion: Is interventional ophthalmology the way forward? *Br. J. Ophthalmol.* **90**, 627–639 (2006)
54. Shi, Y., Karl, W.C.: Real-time tracking using level sets. *IEEE Int. Conf. Computer Vision and Pattern Recognition* **2**, 34–41 (2005)
55. Shonat, R., Kight, A.: Oxygen tension imaging in the mouse retina. *Ann. Biomed. Eng.* **31**, 1084–1096 (2003)
56. Smith, G., Atchison, D.A.: *The eye and visual optical instruments*. Cambridge University Press, Cambridge (1997)
57. Snead, M.P., Rubinstein, M.P., Jacobs, P.M.: The optics of fundus examination. *Sur. Ophthalmol.* **36**(6), 439–445 (1992)
58. Sun, Y., Duthaler, S., Nelson, B.J.: Autofocusing in computer microscopy: selecting the optimal focus algorithm. *J. Microsc. Res. Tech.* **65**(3), 139–149 (2004)
59. Syms, R.R.A., Yeatman, E.M., Bright, V.M., Whitesides, G.M.: Surface tension-powered self-assembly of microstructures—the state-of-the-art. *J. Microelectromech. Syst.* **12**(4), 387–417 (2003)
60. Tang, W.M., Han, D.P.: A study of surgical approaches to retinal vascular occlusions. *Arch. Ophthalmol.* **118**, 138–143 (2000)
61. Tjoa, M., Krishnan, S., Kugean, C., Wang, P., Doraiswami, R.: Segmentation of clinical endoscopic image based on homogeneity and hue. *IEEE Int. Conf. Engineering in Medicine and Biology* pp. 2665–2668 (2001)
62. Tunay, I.: Modeling magnetic catheters in external fields. In: *Proc. IEEE Int. Conf. Engineering in Medicine and Biology Society*, pp. 2006–2009 (2004)
63. Volk, D.A.: Indirect ophthalmoscopy lens for use with split lamp or other biomicroscope (1998). U.S. Patent 5,706,073
64. White, F.M. (ed.): *Fluid Mechanics*, 3rd edn. McGraw-Hill Inc., New York (1994)
65. Yang, G., Gaines, J.A., Nelson, B.J.: Optomechatronic design of microassembly systems for manufacturing hybrid microsystems. *IEEE Trans. Ind. Electron.* **52**(4), 1013–1023 (2005)

66. Yesin, K.B., Vollmers, K., Nelson, B.J.: Modeling and control of untethered biomicro-robots in a fluidic environment using electromagnetic fields. *Int. J. Rob. Res.* **25**(5-6), 527–536 (2006)
67. Zhang, L., Abbott, J.J., Dong, L.X., Kratochvil, B.E., Bell, D., Nelson, B.J.: Artificial bacterial flagella: Fabrication and magnetic control. *Appl. Phys. Lett.* **94**(064107) (2009)